Wave scattering from cylindrical fluid inclusions in an elastic medium and determination of effective medium properties

by

Henry A. Laible

B. S., Ocean Engineering, United States Naval Academy
(1987)

Submitted in partial fulfillment of the
requirements for the dual degrees of

Ocean Engineer

at the

MASSACHUSETTS INSTITUTE OF TECHNOLOGY

and the

WOODS HOLE OCEANOGRAPHIC INSTITUTION

and

Master of Science in Ocean Engineering

at the

MASSACHUSETTS INSTITUTE OF TECHNOLOGY

September 1995

Author _____

Department of Ocean Engineering, MIT and the
MIT-WHOI Joint Program in Oceanographic Engineering

Certified by _____

Dr. Subramaniam D. Rajan
Associate Scientist, Woods Hole Oceanographic Institution
Thesis Supervisor

Accepted by _____

Professor Arthur B. Baggeroer, Chairman
Joint Committee for Oceanographic Engineering
Massachusetts Institute of Technology and the
Woods Hole Oceanographic Institution

Wave scattering from cylindrical fluid inclusions in an elastic medium and determination of effective medium properties

by

Henry A. Laible

Submitted to the Massachusetts Institute of Technology/
Woods Hole Oceanographic Institution
Joint Program in Oceanographic Engineering
on August 9, 1995 in partial fulfillment of the
requirements for the dual degrees of

Ocean Engineer

and

Master of Science in Ocean Engineering

Abstract

The goal of this thesis is to be able to predict acoustic wave speeds in sea ice with known concentrations of inhomogeneities. To accomplish this, ice is modeled as a solid in which cylindrical fluid brine channels are embedded. The solution is formulated by deriving the scattering from a single cylindrical fluid-filled inclusion in an attenuating elastic medium. The scattering vs. angle results are shown for a laboratory experiment in which a single water-filled cylindrical inclusion is embedded in polypropylene. Four different radius-to-wavelength ratios of 1.9, 2.4, 8.8 and 11.0 were measured and proved qualitatively consistent with theory. An extension of the single scattering approximation is used to derive effective moduli for multiple fluid-filled cylinders in an elastic medium. The theory assumes the acoustic wavelength in the medium is long compared to the radius of the cylindrical inclusion so that fluctuations in material properties are effectively averaged over. A separate laboratory experiment was conducted using polypropylene to measure compressional wave speeds for different concentrations of inclusions. The experimental results were within 1% of the wave speeds predicted by effective medium theory. The effective compressional wave speeds predicted by this theory were then compared with wave speeds calculated using empirical relations derived from Arctic ice field data. The maximum error between the two is less than 4%. This effective medium theory is extremely useful for acoustic tomography applications and can be expanded to include other inhomogeneity geometries besides cylinders.

Thesis Supervisor: Dr. Subramaniam D. Rajan

Associate Scientist
Woods Hole Oceanographic Institution

Acknowledgements

Writing a thesis is a challenging and rewarding experience because it affords one the opportunity to interact with so many people. The study at hand is a small contribution to the area of underwater acoustics and acoustic tomography which could have not been completed without the expertise of others. Firstly, I would like to thank Dr. S. Rajan for his support and encouragement over the last three years. He made it possible for my wife and I to study at the Woods Hole Oceanographic Institution by taking me on as his graduate student. His life experiences and career as a scientist combined to make him a mentor from whom I have constantly learned. His patience and encouragement when I have seemingly reached dead ends have been invaluable to my growth. I would also like to thank Dr. Dezhang Chu for his willingness to help me with my experimental work and for his open door when I needed to discuss a problem with him. The experimental work could not have been performed without the equipment of Dr. Tim Stanton or the laboratory tank and lab space of Tom Austin. I thank them for allowing me to use their equipment and space. The experimental results could not have been obtained without the software or the computer to acquire the data. I thank Jim Doutt for providing this vital equipment. I want to thank Charlie Corwin for his ideas on how to keep the transducers in place while taking experimental data. Thanks go to Dr. D.J. Tang for his help in answering questions on the theoretical side of this thesis. He and Dan Li were also helpful in taking data when I needed more than two hands. Cynthia Sellers always had a smiling face when I had problems with the computer workstation. My thanks goes to her for keeping the network operating smoothly when it was not necessarily convenient for her. Lastly I want to thank Prof. Rob Fricke who has been my academic advisor at MIT the last three years. He was always willing to listen to me and provide whatever assistance he could.

Our time in Boston is especially memorable because it was a place where we were challenged intellectually and spiritually. We are thankful to our friends in the Graduate Christian Fellowship at MIT and the married couples group at Grace Chapel for their friendship and prayers. They provided a network of friends who were always willing to lend a hand, no matter what the circumstances. They will definitely be missed but always remembered. I would like to thank my in-laws Anne and Bud Turner for their constant support and phone calls, Anje and Tim for making room for us over the holidays, Elaine for her thoughtfulness and prayers and my parents for all of their love and encouragement. Lastly, I want to thank my lovely wife Jennifer, who willingly came to Boston to fulfill one of my dreams and continually sacrificed to put me through graduate school. I am thankful to her for her love, support and encouragement to enjoy the varied activities of historic Boston. Most importantly, I want to thank God for His grace and love because without it, none of this would have been possible.

We arrive at truth, not by reason only, but also by the heart.

Let us weigh the gain and the loss in wagering that God is. Let us consider the two possibilities. If you gain, you gain all; if you lose, you lose nothing. Hesitate not, then, to wager that He is.

– PASCAL
Pensees (1670)

Contents

List of Figures

List of Tables

Chapter 1

Introduction

1.1 Motivations for work

The modeling of acoustic wave propagation in Arctic ice is a challenging problem because of the presence of inhomogeneities such as air pockets and brine channels. As an acoustic wave propagates through ice, its amplitude decreases due to scattering from the inhomogeneities and from attenuation intrinsic to the ice. The travel time of the acoustic wave, as measured from a transmitter to a receiver, fluctuates because of changes in wave speed of the ice caused by the presence of inhomogeneities.

Sea ice is a complicated multi-layered crystalline material (see Fig. 1-1). The top layers consist of loose and compacted snow. The next layer is a transition layer only a few centimeters thick in which the crystalline nature of ice begins to take form. It is in this layer that the preferred orientation of the crystal optic axis (C axis) develops. Beneath the transition layer and extending almost entirely to the bottom of the ice is the columnar zone. In this region the crystalline structure of the ice is aligned such that it is roughly colinear over large distances relative to a typical grain diameter. Brine channels and brine pockets exist in the columnar zone as a result of the freezing process of sea water. The bottom layer is the skeletal layer which is a thin layer at the ice-water interface. This layer has a thickness of the order of a few centimeters and is characterized by the presence of thin ice platelets arranged perpendicular to the C axis of individual crystals [32].

This study models ice as a homogeneous elastic medium in which fluid-filled cylindrical brine channels are embedded. The physics behind scattering from a single fluid inclusion is studied. This work is then expanded to include multiple fluid-filled cylindrical scatterers.

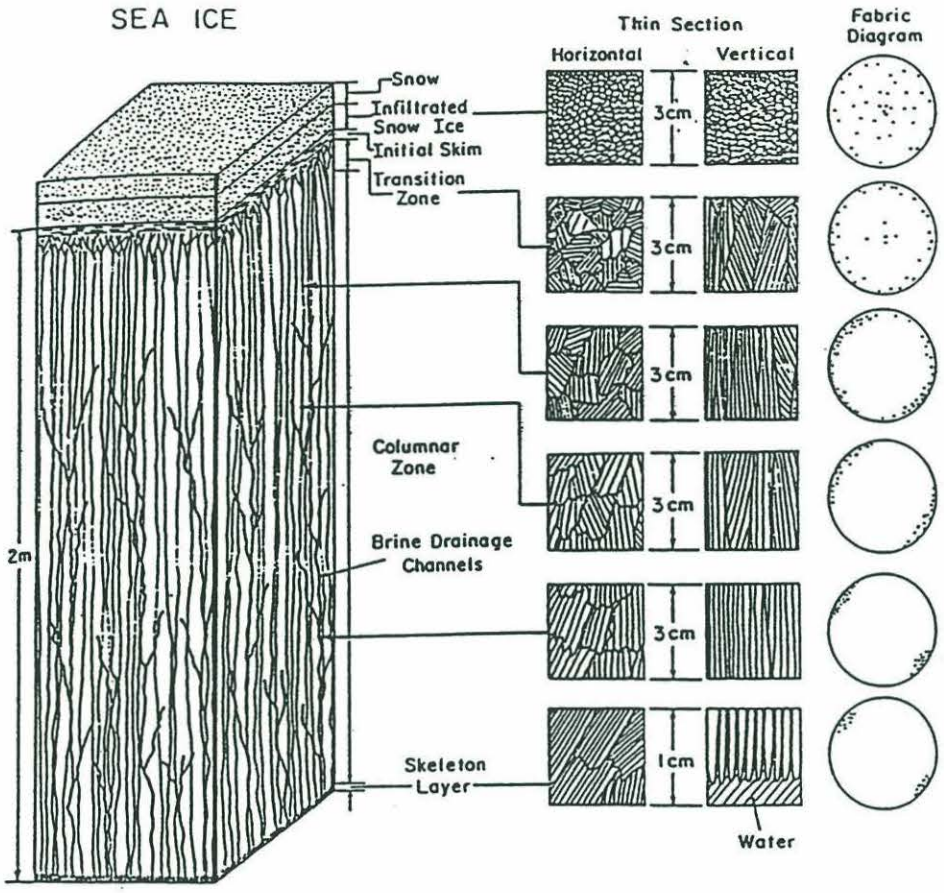

Figure 1-1: Structure of sea ice (Weeks and Ackley, 1982).

To determine the scattering from multiple cylinders, a weak scattering solution is used where the total scattered field is the sum of contributions from individual scatterers. The interaction between individual scatterers is neglected. Further, with the assumption that the acoustic wavelength is much larger than the size of the inclusions, the average material properties can be obtained. These average values are commonly referred to as effective medium properties and the theory behind the derivation of these average values is termed the effective medium theory.

After the theoretical developments are complete, numerical simulations are performed to predict results from laboratory acoustic scattering experiments. The laboratory experiments are conducted using polypropylene as a surrogate for ice. The purpose of the laboratory experiments is to validate the theoretical work.

This thesis provides a unique contribution to acoustic wave propagation in a heteroge-

neous material with cylindrical inclusions such as ice because it allows one to determine the wave speeds in the material for a given concentration of inhomogeneities. The effective medium theory can be used to map regions of ice where high concentrations of such inhomogeneities exist. As an example of this refer to Fig. 1-2 where traveltime acoustic tomography has been used to determine the compressional wave speeds in ice. The regions of high inhomogeneity concentration can be determined using this map of compressional wave speed.

1.2 Overview of thesis

Chapter 2 is devoted to the analytic development of the acoustic scattering from an infinite, fluid-filled cylinder in an elastic matrix taking into account attenuation in the elastic matrix. Chapter 3 is an expansion of the work done in Chap. 2 where low frequency scattering from multiple fluid-filled cylinders is analyzed. The goal of Chap. 3 is to derive a set of analytic equations which will give the effective Lamè parameters and effective density of the elastic matrix. Knowing these, the effective acoustic wave speeds in the material can be derived. Chapter 4 is devoted to the experimental work where the scattering in angle is measured for a single cylindrical inclusion in the elastic matrix. Results are presented for the scattering from cylindrical water-filled inclusions for various radius to acoustic wavelength ratios. Chapter 5 is devoted to experimental work in which the scattering from multiple cylindrical fluid inclusions is measured in order to derive the effective elastic moduli for radius to acoustic wavelength ratios $\ll 1$. Wave speeds are measured for various concentrations of cylindrical fluid inclusions and compared to predictions using effective medium theory. Additionally, wave speeds using the effective medium theory are compared with wave speeds derived from empirical formulas for sea ice. The last section of Chap. 5 shows an application of the effective medium theory to acoustic tomography. Compressional wave speed data from tomographic inversion are used as inputs to effective medium relations to predict regions of high and low concentrations of inhomogeneities. Lastly, Chap. 6 is a summary of the results and conclusion. Recommendations for future research and how the effective medium theory can be expanded are discussed.

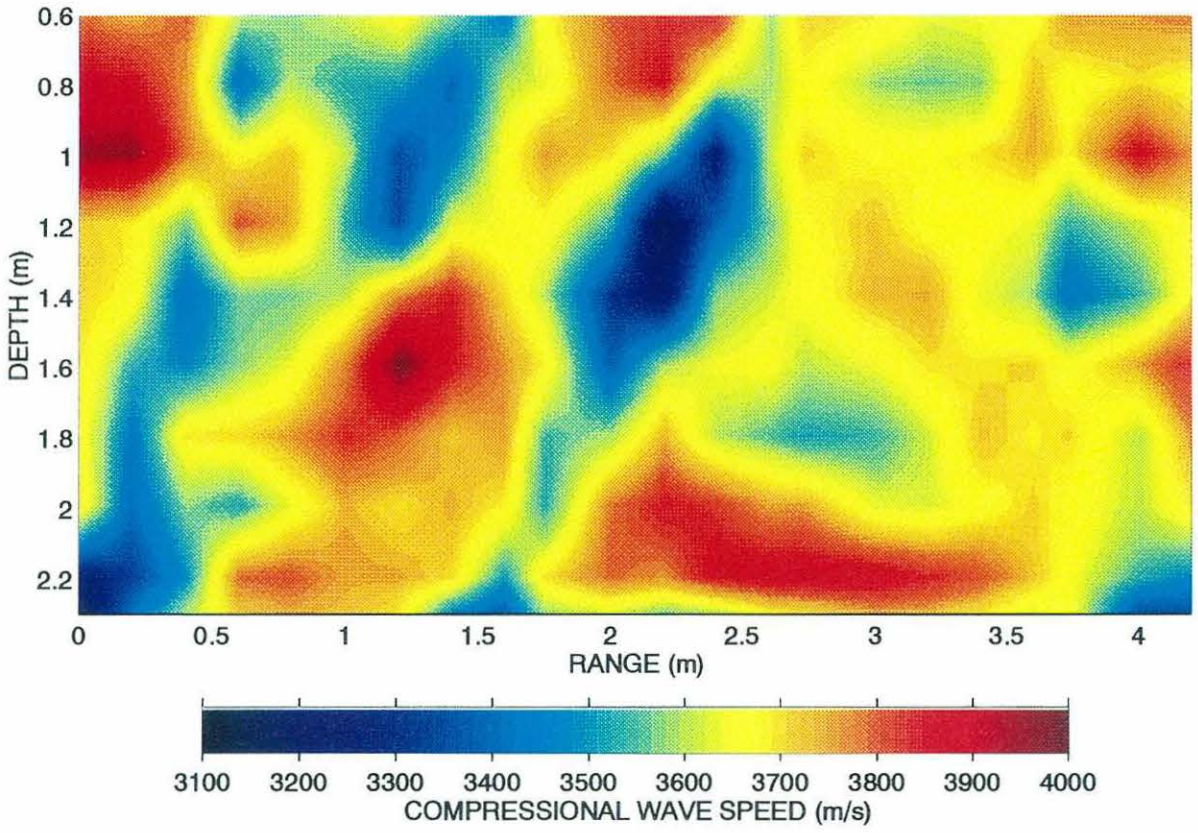

Figure 1-2: Compressional wave speeds from tomographic inversion (Rajan *et al.*, 1993).

Chapter 2

Scattering theory

In this chapter a review of elastic wave scattering is given and the analytic equations governing acoustic wave scattering from a single fluid-filled cylindrical inclusion in an elastic matrix are derived.

2.1 Elastic scattering review

The study of acoustic wave scattering has been an important topic in the past and continues to be an area of concentrated research. Lord Rayleigh [26] first investigated the scattering of sound. Parallel to his study, others were investigating wave propagation in elastic media. Love's treatise on the mathematical theory of elasticity [21] provides an excellent historical background on elastic wave propagation. A classic paper which studies the acoustic scattering from solid cylinders and spheres was presented by Faran[10]. He developed the scattering theory for a plane wave normally incident upon a solid elastic cylinder and sphere in a fluid medium. Both the transmitted shear and compressional waves in the cylinder as well as the scattered compressional wave are considered. White [33] studied the scattering of both plane compressional and shear waves incident upon a solid cylindrical discontinuity in an isotropic solid. He also derived the scattering equations for a fluid-filled cylindrical bore. Kim *et al.* [17] dealt with scattering from a cylindrical cavity in an elastic medium by taking into account attenuation in the medium. The authors determined the angular distribution of the scattered field and calculated the time domain impulse responses for the scattered displacement field. Another paper which takes into account attenuation is presented by Beattie *et al.* [5]. However, they solve the problem of ultrasonic backscat-

tering from a solid cylindrical scatterer in a solid elastic matrix. The formulation in this thesis will be for a fluid cylindrical inclusion in an attenuating elastic matrix. Although the theoretical derivation for a fluid inclusion was presented by White [33], attenuation was not accounted for in the elastic matrix. Additionally, numerical simulations are presented for various radius-to-wavelength ratios and several values of compressional and shear attenuation.

2.2 Analytical development

The following derivation of scattering is based on a series solution to the wave equation. The formulation follows along the lines of that presented by Faran. [10] The purpose of this development is to arrive at the scattering coefficients so that the angular scattered displacement field can be calculated. The following assumptions are made in this derivation:

1. An infinitely long fluid cylinder is embedded in an infinite elastic matrix
2. A compressional plane wave is incident normal to the axis of the cylindrical inclusion.

The displacement vector of a wave in a solid is represented by certain solutions of the equation of motion. The equation of motion for an isotropic elastic medium is [2]

$$(\lambda + 2\mu)\nabla\nabla \cdot \vec{u} + \mu\nabla^2\vec{u} = \rho\frac{\partial^2\vec{u}}{\partial t^2} \tag{2.1}$$

where λ and μ are Lamé parameters, ρ is the density of the solid and $\vec{u}$ is the displacement vector. Because the medium is solid, it can support two types of waves: compressional and shear. To arrive at solutions to Eq. (2.1) where the compressional and shear waves can be studied independently, the scalar and vector potentials Φ and $\mathbf{\Psi}$ are introduced such that

$$\vec{u} = \nabla\Phi + \nabla \times \mathbf{\Psi}. \tag{2.2}$$

Φ corresponds to the compressional displacement potential and $\mathbf{\Psi}$ corresponds to the shear displacement potential. After carrying out the mathematics, the displacement vector (2.2) is found to satisfy

$$\nabla^2\Phi = \frac{\rho}{\lambda + 2\mu}\frac{\partial^2\Phi}{\partial t^2} \tag{2.3}$$

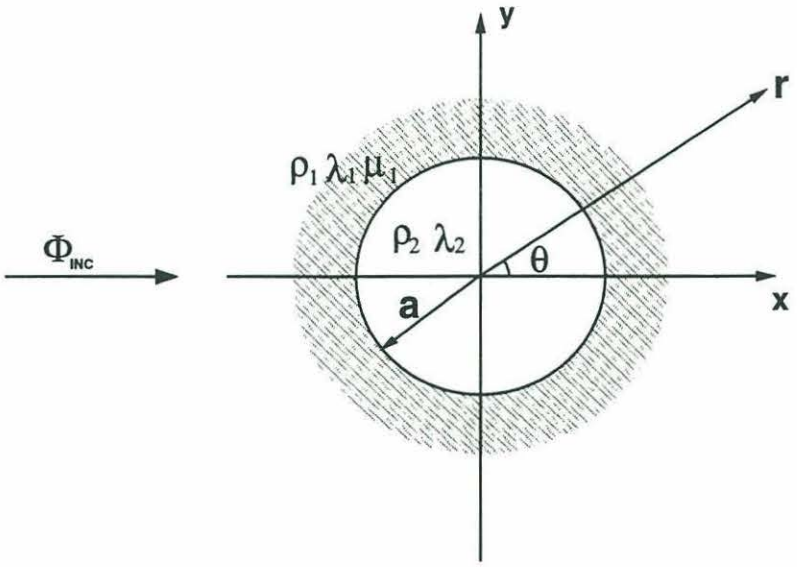

Figure 2-1: Geometry for a compressional wave incident on a cylindrical fluid-inclusion of radius a. The elastic matrix is type 1 material and the inclusion is type 2.

and

$$\nabla^2 \Psi = \frac{\rho}{\mu} \frac{\partial^2 \Psi}{\partial t^2}. \tag{2.4}$$

Eqs. (2.3) and (2.4) are called the uncoupled wave equations and correspond to compressional and shear waves respectively. The compressional and shear wave speeds are defined to be

$$c_p^2 = \frac{\lambda + 2\mu}{\rho} \tag{2.5}$$

and

$$c_s^2 = \frac{\mu}{\rho}. \tag{2.6}$$

Figure 2-1 shows the geometry of the problem for a compressional plane wave in an elastic medium normally incident upon a fluid inclusion. Note that the solid elastic matrix is labeled as material 1 and the fluid inclusion as material 2. Due to conversion at the solid-fluid interface, scattered compressional and shear waves are produced. Since the fluid is only able to support compressional waves, the transmitted wave is a compressional wave. Figure 2-2 visualizes the physics of mode conversion for this problem. Because the acoustic scattering is from a cylindrical inclusion, a cylindrical coordinate system is chosen to make the analysis simpler. The coordinate system is defined by:

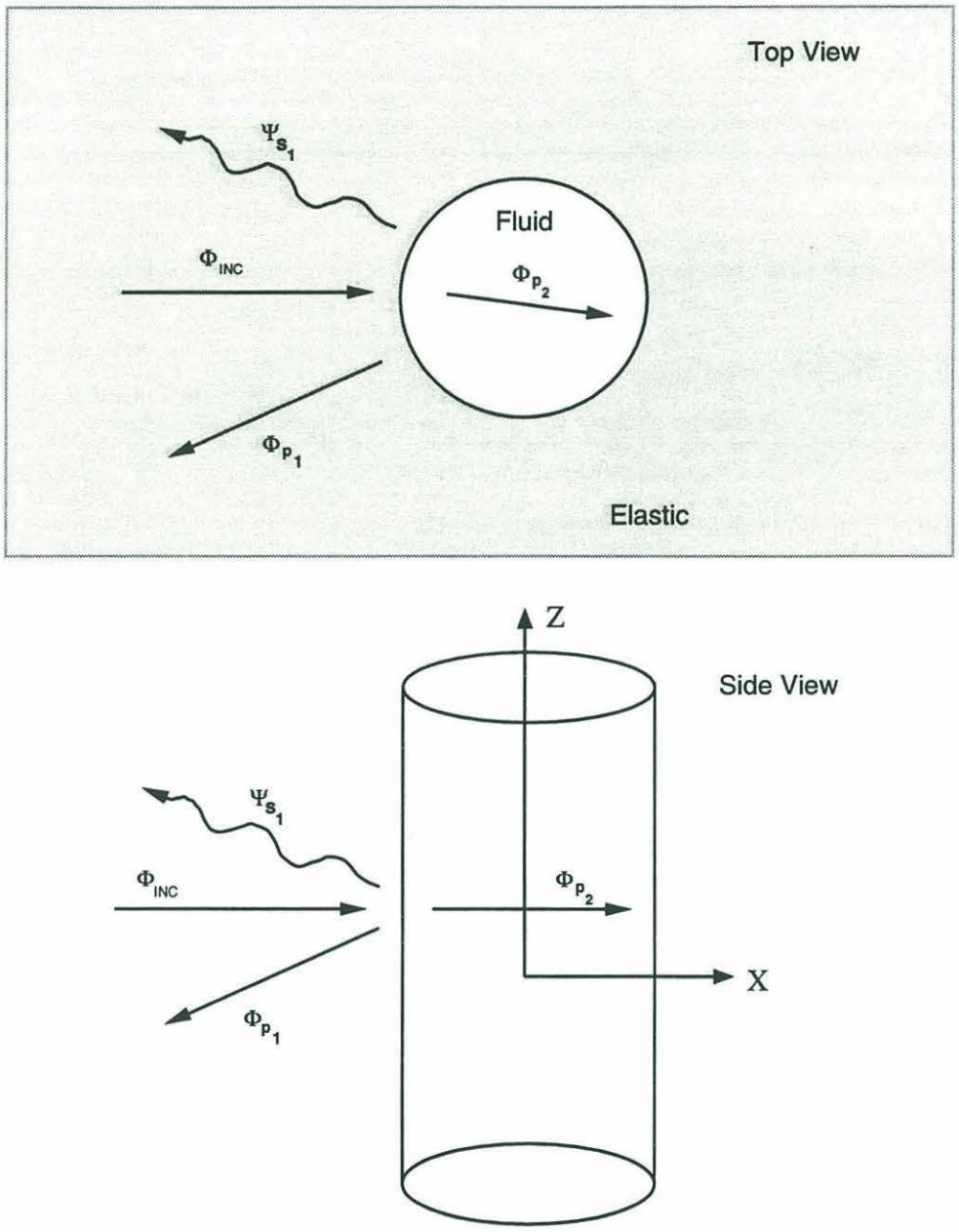

Figure 2-2: Top and side view showing mode conversion for P wave incident normal to cylinder axis.

$$x = r\cos\theta, \quad y = r\sin\theta, \quad \text{and} \quad z = z.$$

r is the radial distance from the center of the inclusion and θ is the angle measured counter-clockwise from the positive X axis shown in Fig. 2-1.

If the incident field, Φ_{INC}, is a plane wave then

$$\Phi_{INC} = \Phi_o e^{i(kr\cos\theta - \omega t)}$$

where Φ_o is the incident amplitude, $k = \omega/c$ is the wavenumber, w is the angular frequency, c is the wavespeed in the material, and t is time. The plane wave is decomposed into an infinite sum of cylindrical Bessel functions in order to match the boundary conditions at the inclusion surface. The incident potential can be written as [23]

$$\Phi_{INC} = \sum_{n=0}^{\infty} \epsilon_n i^n J_n(k_{p_1} r)\cos(n\theta)e^{-i\omega t} \tag{2.7}$$

where Φ_o has been normalized to unity, k_{p_1} is the wavenumber ω/c_{p_1} in medium one, ϵ_n is the Neumann coefficient ($\epsilon_0 = 1$ and $\epsilon_n = 2$ for n ≥ 1), i is $\sqrt{-1}$ and J_n is the cylindrical Bessel function of the first kind of order n.

2.2.1 Scattered compressional wave

The scattered compressional waves must satisfy Eq. (2.3). Assuming a monochromatic incident wave, the solution can be written as:

$$\Phi = \phi(r,\theta)e^{-i\omega t}. \tag{2.8}$$

Substituting this into Eq. (2.3), we get the well known Helmholtz equation,

$$\nabla^2\phi(r,\theta) + k_{p_1}^2\phi(r,\theta) = 0 \tag{2.9}$$

where k_{p_1} is the longitudinal wavenumber ω/c_{p_1}. If a general solution to Eq. (2.9) is assumed of the form

$$\phi = R(r)\Theta(\theta) \tag{2.10}$$

the process of separation of variables leads to two separate equations:

$$r^2\frac{\partial^2 R}{\partial r^2} + r\frac{\partial R}{\partial r} + (k_{p_1}^2 r^2 - n^2)R = 0 \tag{2.11}$$

$$\frac{\partial^2 \Theta}{\partial \theta^2} + n^2\Theta = 0 \tag{2.12}$$

where n is an arbitrary separation constant. Eq. (2.11) is Bessel's equation whose solution is of the form:

$$R(r) = A_{n_1} H_n^{(1)}(k_{p_1} r) + A_{n_2} H_n^{(2)}(k_{p_1} r). \tag{2.13}$$

The solution to Eq. (2.12) is:

$$\Theta(\theta) = B_{n_1}\cos(n\theta) + B_{n_2}\sin(n\theta) \tag{2.14}$$

where A_{n_1}, A_{n_2}, B_{n_1} and B_{n_2} are constants to be determined by boundary conditions and $H_n^{(1)}$ and $H_n^{(2)}$ are Hankel functions of the first and second kind respectively. Choosing the scattered compressional wave to be the general series:

$$\Phi = \sum_{n=0}^{\infty}(A_{n_1} H_n^{(1)}(k_{p_1} r) + A_{n_2} H_n^{(2)}(k_{p_1} r))(B_{n_1}\cos(n\theta) + B_{n_2}\sin(n\theta))e^{-i\omega t} \tag{2.15}$$

and writing out the asymptotic representations of the Hankel functions for large values of k_{p_1}r, the scattered potential can be simplified. For a fixed n, the following Bessel function relations hold true [1]:

$$H_n^{(1)}(k_{p_1} r) \sim \left(\frac{2}{\pi k_{p_1} r}\right)^{\frac{1}{2}} e^{i(k_{p_1} r - \frac{1}{2}n\pi - \frac{\pi}{4})} \quad \text{as} \quad k_{p_1} r \to \infty \tag{2.16}$$

$$H_n^{(2)}(k_{p_1} r) \sim \left(\frac{2}{\pi k_{p_1} r}\right)^{\frac{1}{2}} e^{-i(k_{p_1} r - \frac{1}{2}n\pi - \frac{\pi}{4})} \quad \text{as} \quad k_{p_1} r \to \infty \tag{2.17}$$

Outgoing scattered waves are of interest, but $H_n^{(2)}(k_{p_1} r)$ will yield an incoming wave due to the choice of an $e^{-i\omega t}$ time dependence. Hence the coefficient A_{n_2} must be equal to

zero.

For the angular dependence term in Eq. (2.14), the scattered displacement potential must be symmetric about $\theta = 0$ so B_{n_2} must be equal to zero. Combining the terms together yields the following simplified scattered compressional potential:

$$\Phi_{c_1} = \sum_{n=0}^{\infty} A_n H_n^{(1)}(k_{p_1} r) \cos(n\theta) e^{-i\omega t}. \tag{2.18}$$

The coefficients A_n are the scattering coefficients associated with the scattered compressional wave and are determined from the boundary conditions at the inclusion-solid boundary.

2.2.2 Scattered Shear Wave

The derivation of the scattered vector potential is analogous to that of the scattered compressional potential. The vector potential Ψ_{s_1} here corresponds to a vertically polarized (SV) shear wave since we have a compressional (P) wave incident. A horizontally polarized (SH) wave is not possible since the reflected transverse wave must have a displacement vector polarized in the same plane as the incident compressional wave. For a P wave incident normal to the axis of the cylinder, the scattered SV and P wave propagating vectors are parallel to the plane of the propagating vector for the incident P wave. The SV wave can be simplified from a vector potential to a scalar potential since we have an incident plane wave which is *normal* to the cylindrical inclusion. The vector potential Ψ_{s_1} can be reduced to a scalar because the motion is parallel to the z axis. The only non-zero component of the shear potential is the z component and is given by:

$$\Psi_{s_1} = \sum_{n=0}^{\infty} B_n H_n^{(1)}(k_{s_1} r) \sin(n\theta) e^{-i\omega t}. \tag{2.19}$$

Notice that the $\sin(n\theta)$ terms appears vice $\cos(n\theta)$. The reason for this is that the displacement potential calculated from Eq. (2.2) must be symmetric about $\theta = 0$. The coefficients B_n in Eq. (2.19) are the scattering coefficients for the shear wave and are determined from boundary conditions at the inclusion-solid interface.

2.2.3 Transmitted Compressional Wave

As discussed earlier, the fluid cylindrical inclusion can only support compressional waves so the transmitted wave will be of the form:

$$\Phi_{c_2} = \sum_{n=0}^{\infty} \left\{ C_n H_n^{(1)}(k_{p_2} r) + D_n H_n^{(2)}(k_{p_2} r) \right\} \cos(n\theta) e^{-i\omega t}.$$

However $H_n^{(1,2)}(k_{p_2} r)$ can be written in terms of Bessel functions of the first and second kind:

$$H_n^{(1,2)}(k_{p_2} r) = J_n(k_{p_2} r) \pm i Y_n(k_{p_2} r). \tag{2.20}$$

$Y_n(k_{p_2} r)$ is not finite at the origin $r = 0$ so in order for Φ_{c_2} to exist, the scattering coefficient for $Y_n(k_{p_2} r)$ must be set equal to zero, i.e. $D_n = C_n$. This simplifies to the final solution for Φ_{c_2}:

$$\Phi_{c_2} = \sum_{n=0}^{\infty} C_n J_n(k_{p_2} r) \cos(n\theta) e^{-i\omega t}. \tag{2.21}$$

Once again, the C_n's are the scattering coefficients to be determined from the boundary conditions.

2.2.4 Including attenuation in the scattering problem

Most scattering problems assume that we have an ideal fluid/solid so that attenuation can be neglected. However, this is not generally the case. In this scattering problem, attenuation is of interest because of its application to the Arctic ice problem. Ice itself is highly attenuating to sound and depends upon frequency. As previously stated, others have included the effects of attenuation in their scattering experiment [5, 17] by making the wavenumber k a complex quantity.

$$k = \omega/c + i\alpha \tag{2.22}$$

ω is the radial frequency, c is the wave speed in the material (either shear or compressional) and α is the attenuation. Generally, the frequency dependence of attenuation for a solid is linear. Specifically, α can be written as [5]

$$\alpha = \gamma f \tag{2.23}$$

where γ is the attenuation coefficient in neper m^{-1} f^{-1} and f is the frequency in Hz. Making the wavenumber complex makes solving the Bessel and Hankel functions non-trivial. A discussion later in this chapter of how to numerically solve these functions with complex arguments is provided.

2.3 Solution to the scattering problem

In this section the solution is derived for acoustic scattering from cylindrical fluid inclusions in an elastic matrix. The scattering coefficients which were defined in Secs. 2.2.1, 2.2.2, and 2.2.3 are determined. Solving for these coefficients requires knowing the incident field as well as the field inside the scatterer. Matching boundary conditions enables one to solve for the scattering coefficients.

2.3.1 Boundary conditions

The motion of particles at the solid-fluid interface dictates the appropriate boundary conditions. The boundary conditions for a cylindrical fluid inclusion in a surrounding elastic matrix are fairly straightforward and have been presented by others [5, 17, 33]. Since the scattering problem in this thesis deals with a fluid inclusion, only three scattering coefficients are solved for. Hence, three boundary conditions are needed to solve for the A_n's, B_n's, and C_n's. The A_n's are the scattered compressional coefficients, the B_n's are the scattered shear coefficients and the C_n's are the transmitted compressional coefficients. The boundary conditions must satisfy the following conditions:

1. continuity of radial particle displacement
2. continuity of radial stress
3. vanishing shear stress at the boundary.

Mathematically we can write these as:

$$u_r^{inc} + u_r^{scatt} = u_r^{trans} \tag{2.24}$$

$$\tau_{rr}^{inc} + \tau_{rr}^{scatt} = \tau_{rr}^{trans} \tag{2.25}$$

$$\tau_{r\theta}^{inc} + \tau_{r\theta}^{scatt} = 0. \tag{2.26}$$

2.3.2 Equations in cylindrical coordinates

Before proceeding with the solutions for the scattering coefficients, it would be helpful to write out the particle displacements and shear stresses in cylindrical coordinates. From Eq. (2.2) the particle displacement is:

$$\vec{u} = \nabla\Phi + \nabla \times \mathbf{\Psi}.$$

The gradient operator ∇ is defined in cylindrical coordinates by: [15]

$$\nabla = \frac{\partial}{\partial r}\hat{u}_r + \frac{1}{r}\frac{\partial}{\partial \theta}\hat{u}_\theta + \frac{\partial}{\partial z}\hat{u}_z \tag{2.27}$$

where $\hat{u}_r$, $\hat{u}_\theta$, and $\hat{u}_z$ are unit vectors in the r, θ, and z directions respectively.
The divergence operator in cylindrical coordinates is given by:

$$\nabla \cdot \mathbf{F} = \frac{1}{r}\frac{\partial(rF_r)}{\partial r} + \frac{1}{r}\frac{\partial F_\theta}{\partial \theta} + \frac{\partial F_z}{\partial z} \tag{2.28}$$

where F_r, F_θ, and F_z are the components of vector $\mathbf{F}$ in the r, θ, and z directions.
The curl of a vector in cylindrical coordinates is: [15]

$$\nabla \times \mathbf{F} = \frac{1}{r}\begin{vmatrix} \hat{u}_r & r\hat{u}_\theta & \hat{u}_z \\ \frac{\partial}{\partial r} & \frac{\partial}{\partial \theta} & \frac{\partial}{\partial z} \\ F_r & F_\theta & F_z \end{vmatrix}. \tag{2.29}$$

The radial particle displacement, u_r and the displacement in the θ direction, u_θ are defined by [2]

$$u_r = \frac{\partial\Phi}{\partial r} + \frac{1}{r}\frac{\partial\Psi_z}{\partial \theta} \tag{2.30}$$

$$u_\theta = \frac{1}{r}\frac{\partial\Phi}{\partial \theta} - \frac{\partial\Psi_z}{\partial r}. \tag{2.31}$$

Because of the symmetry of the problem, the vector displacement has been reduced to a scalar since the vector potential Ψ has components only in the z direction. Hence Ψ is written with the subscript z to denote that this is the only component that is non-zero.

The stress-strain relations in terms of Lamé parameters are [2]

$$\tau_{rr} = \lambda \nabla \cdot \vec{u} + 2\mu\epsilon_r \tag{2.32}$$

$$\tau_{r\theta} = 2\mu\epsilon_{r\theta} \tag{2.33}$$

where

$$\epsilon_r = \frac{\partial u_r}{\partial r}$$

$$2\epsilon_{r\theta} = \frac{\partial u_\theta}{\partial r} - \frac{u_\theta}{r} + \frac{1}{r}\frac{\partial u_r}{\partial \theta}$$

and the divergence of the particle displacement is:

$$\nabla \cdot \vec{u} = \frac{\partial u_r}{\partial r} + \frac{u_r}{r} + \frac{1}{r}\frac{\partial u_\theta}{\partial \theta}.$$

Substituting these relations into the boundary conditions and evaluating them at the cylinder boundary $r = a$ yields three equations in three unknowns. Writing the equations in the form of $XB = D$ where X is a 3x3 matrix and B and D are 3x1 vectors. The solution can be written in this format as shown below.

$$\begin{bmatrix} x_{11} & x_{12} & x_{13} \\ x_{21} & x_{22} & x_{23} \\ x_{31} & x_{32} & x_{33} \end{bmatrix} \begin{bmatrix} A_n \\ B_n \\ C_n \end{bmatrix} = \begin{bmatrix} D_1 \\ D_2 \\ D_3 \end{bmatrix} \tag{2.34}$$

where the elements of the X matrix and D vector are given by:

$$
\begin{aligned}
x_{11} &= k_{p1} a H_n'(k_{p1}a) \\
x_{12} &= n H_n(k_{s1}a) \\
x_{13} &= -k_{p2} a J_n'(k_{p2}a)
\end{aligned}
$$

$$
\begin{aligned}
x_{21} &= H_n(k_{p1}a)(2n^2 - k_{s1}^2 a^2) - 2k_{p1} a H_n'(k_{p1}a) \\
x_{22} &= 2n(k_{s1} a H_n'(k_{s1}a) - H_n(k_{s1}a)) \\
x_{23} &= \frac{\rho_2}{\rho_1} k_{s1}^2 a^2 J_n(k_{p2}a)
\end{aligned}
$$

$$
\begin{aligned}
x_{31} &= 2n(H_n(k_{p1}a) - k_{p1} a H_n'(k_{p1}a)) \\
x_{32} &= 2k_{s1} a H_n'(k_{s1}a) + (k_{s1}^2 a^2 - 2n^2) H_n(k_{s1}a) \\
x_{33} &= 0
\end{aligned}
$$

$$
\begin{aligned}
D_1 &= -\epsilon_n i^n k_{p1} a J_n'(k_{p1}a) \\
D_2 &= -\epsilon_n i^n \{(2n^2 - k_{s1}^2 a^2) J_n(k_{p1}a) - 2k_{p1} a J_n'(k_{p1}a)\} \\
D_3 &= \epsilon_n i^n 2n(k_{p1} a J_n'(k_{p1}a) - J_n(k_{p1}a)).
\end{aligned}
$$

The primes on the Hankel and Bessel functions represent a derivative with respect to their arguments. The only unknowns are the scattering coefficients A_n, B_n, and C_n. As stated before, only the scattered compressional coefficient A_n will be involved in the present study. Solving for A_n is straightforward which does not require a matrix inversion of the X matrix. Using Cramer's rule, A_n can be written in terms of the matrix determinants.

$$
A_n = \frac{\begin{vmatrix} D_1 & x_{12} & x_{13} \\ D_2 & x_{22} & x_{23} \\ D_3 & x_{32} & x_{33} \end{vmatrix}}{\text{DET } |\text{X}|} \tag{2.35}
$$

where the determinant of the X matrix can be written in terms of its elements

$$
\text{DET } |\text{X}| = x_{11}(x_{22}x_{33} - x_{32}x_{23}) - x_{12}(x_{21}x_{33} - x_{31}x_{23}) + x_{13}(x_{21}x_{32} - x_{31}x_{22}). \tag{2.36}
$$

A_n can be simplified since $x_{33} = 0$. The simplified form is:

$$
A_n = \frac{x_{23}(x_{12}D_3 - D_1 x_{32}) + x_{13}(D_2 x_{32} - D_3 x_{22})}{x_{23}(x_{12}x_{31} - x_{11}x_{32}) + x_{13}(x_{21}x_{32} - x_{31}x_{22})}. \tag{2.37}
$$

2.4 Numerical Results

Having derived the analytic solution to the scattered compressional wave problem, the next step is to compute the scattering in angle for a compressional plane wave incident on a fluid inclusion. The computer code is written in Fortran 77 and uses an input file where one can specify:

- the frequency of the plane wave,
- size of the fluid inclusion,
- compressional and shear wave speeds of the solid matrix,
- compressional wave speed in the fluid,
- compressional and shear wave attenuations in the solid,
- densities of the matrix and fluid,
- angular increment over which to compute the scattering, and
- the term to which the infinite series is to be truncated.

Attenuation is incorporated by making the wavenumber complex as discussed in Sec. 2.2.4. The difficulty in computing the scattering coefficient A_n lies in computing the Bessel and Hankel functions with complex arguments. Amos [4] discusses the complexity of computing Bessel functions when the argument is complex. The problems of correct scaling to prevent underflow and overflow, the problem of analytic continuation (continuity across the negative real axis) and whether to use asymptotic expansion or forward or backward recurrence relations for the Bessel functions present themselves when dealing with complex arguments.

In another paper, Du Toit [9] performs numerical computations for Bessel functions with complex arguments however the algorithms are not readily suitable for implementation. A recent PhD thesis by Ricks [27] computes the scattering from an elastic cylinder. In his numerical simulations, he calculates Bessel functions with complex arguments using the subroutines of Amos [4]. The subroutines compute the Bessel and Hankel functions in double precision and are written in Fortran 77. The numerical simulations in this study utilize the subroutines which Ricks has compiled for use on a Unix-based workstation.

Inputs to numerical model	
Frequency (kHz)	160
Inclusion radius (m)	2.5e-04
Radius of solid matrix (m)	0.15
Compressional wave speed in inclusion (m/s)	1490
Compressional wave speed in solid matrix (m/s)	2528
Shear wave speed in solid matrix (m/s)	1270
Density of matrix (kg/m^3)	913
Density of fluid inclusion (kg/m^3)	1000
Angle increment (deg)	0.5
Truncation number	40

Table 2.1: Actual inputs to numerical model for $ka = 0.1$. For ka values of 1.0 and 10.0, the frequency was kept constant and the inclusion radius changed.

2.4.1 Angular Dependence of the Scattered Displacement Field

The scattering displacement in the radial direction for a single fluid filled cylinder was computed for an incident compressional plane wave at various frequencies and inclusion radii to study the effects of variations in ka. The solution to the scattered displacement field in the radial direction is:

$$u_r^{scatt} = \sum_{n=0}^{\infty} \left[A_n k_{p_1} H_n'(k_{p_1} r) + B_n \frac{n}{r} H_n(k_{s_1} r) \right] \cos(n\theta) \tag{2.38}$$

The A_n and B_n coefficients were calculated and then substituted in Eq. (2.38) to derive the scattered displacement potential in the radial direction.

The first trial was done at 160 kHz for three different fluid-filled inclusion radii and varying compressional attenuations. For all three ka values, the following compressional attenuations were used: 0, .1, 10 nepers/m. A value for shear attenuation was chosen as three times that of compressional attenuation based on relationships between compressional and shear attenuation in ice. However, in the numerical simulations shear attenuation had little or no effect on the scattered radial displacement field because this type of attenuation affects tangential displacement. Table 2.1 shows the typical input parameters for case 1. The radial distance r from the center of the cylindrical inclusion was chosen as 15 cm

since the experimental work was conducted on a polypropylene rod of this radius. The value of the compressional wave speed of the solid (c_{p_1}) was chosen based on laboratory measurements made on polypropylene. The shear wave speed (c_{s_1}) could not be measured so it was chosen based on measurements made by others[13]. The compressional wave speed of the fluid inclusion (c_{p_2}) was chosen because it is representative of a freshwater value. For kr values of interest, the infinite series in Eq.(2.38) was truncated at 40 terms because contributions to the scattered displacement field for higher order terms were negligible. Additionally, this value was chosen to compare to the results of Kim *et al.*[17]. The results for the numerical model are shown in Fig. 2-3.

The effect of attenuation and parameter ka can be seen by the shape of the scattering pattern. At low ka values, the scattering pattern has a dipole-like shape which is indicative of Rayleigh scattering ($ka \ll 1$) for a cylinder. As the ka value increases, we see the scattered field is more concentrated in the forward direction ($\theta = 0°$). This is representative of the geometric scattering region where the scattered field in the forward direction interferes with the incident field to produce a shadow zone in the forward scattering direction. For all three values of ka, we see the amplitude is greatest without attenuation. As attenuation increases, the scattered amplitude decreases as is expected.

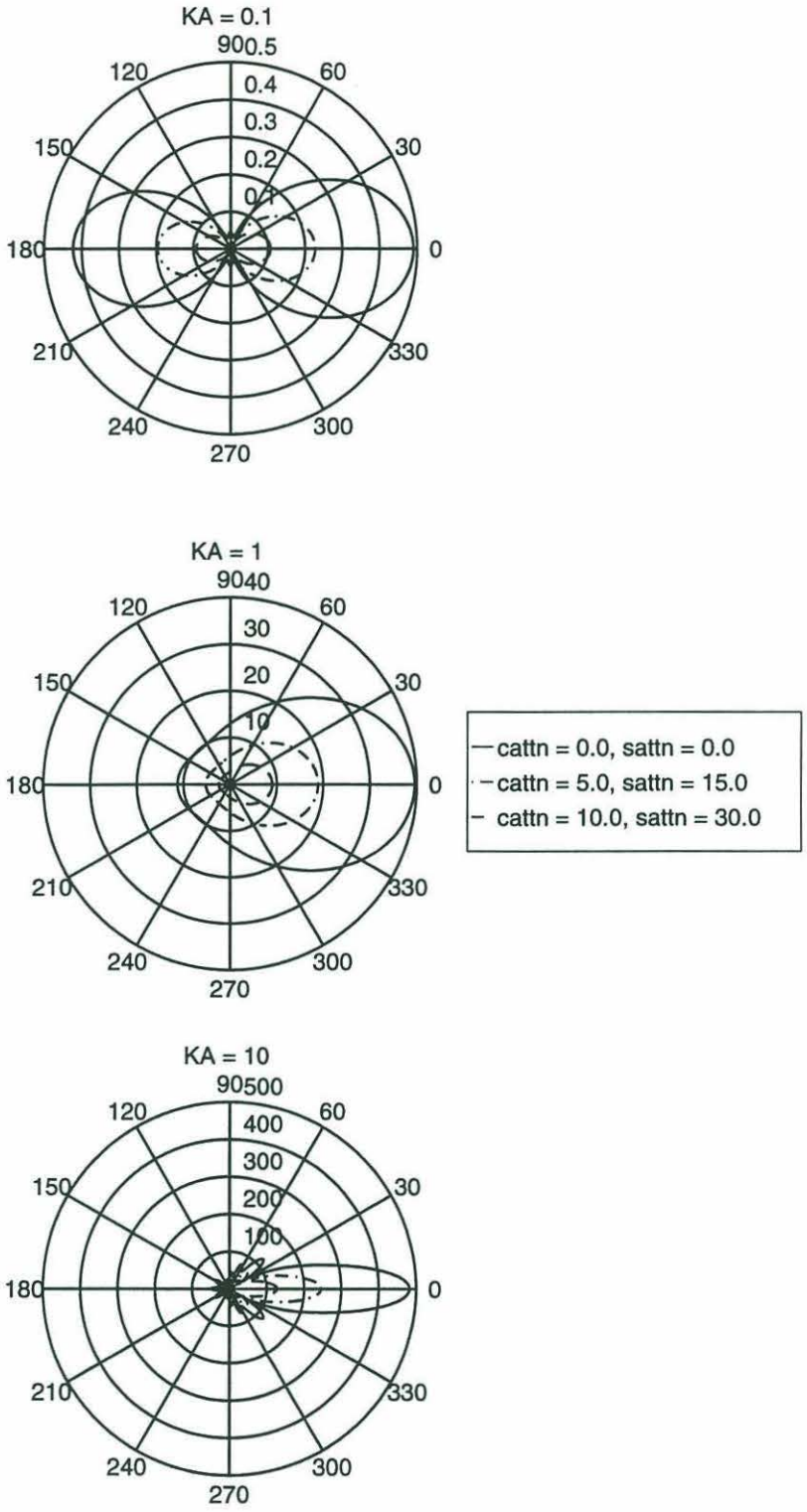

Figure 2-3: Computed scattered displacement field for compressional attenuations of 0, 5, and 10 Neper/m and shear attenuations of 0, 15, and 30 Neper/m for top: $ka = 0.1$, middle: $ka = 1.0$, and bottom: $ka = 10.0$.

Chapter 3

Effective Medium Theory

In this chapter the concept of an effective medium is used to infer average elastic constants of a material with inhomogeneities. Brine channels are examples of cylindrical inhomogeneities which occur in sea ice. The reason for this study is to be able to predict the concentration of these inhomogeneities from a measurement of the wave speed. The background of effective medium theory is described and two theories which are widely used in the field of seismology and non-destructive evaluation are examined. The theory developed by Kuster and Toksöz for spherical inclusions is expanded for the case in which fluid-filled cylindrical inclusions are embedded in an elastic matrix.

3.1 History

The concept of an effective medium applies when acoustic waves propagate through a medium made up of two homogeneous materials. Instead of attempting to define the exact quantity and location of inhomogeneities within a material, we can define an effective medium whose acoustic properties are the same as those of the aggregate of the two phase materials. In traveltime acoustic tomography, general properties such as compressional and shear wave speed are determined. These properties are spatial averages which are averaged over the acoustic wavelength. The effective medium theory is also an average of the material properties which make up a quasi-homogeneous mixture.

The effective medium theory is not new and dates back to the early 1960's where much work was done in the area of seismic wave propagation. The goal of the work was to be able to understand the differences in elastic wave velocities and try to predict if these differences

were due to crack formation preceding an earthquake. The rocks are modeled as partially or fully fluid saturated in which the elastic waves propagate. The solid rock is considered a homogeneous elastic phase in which inclusions of another phase are embedded.

The concept of an effective medium has been important in the study of composite materials. Ultrasonic and non-destructive evaluation employ the concept of effective medium theory in order to determine flaw concentration in a material.

An excellent review of the different methods of computing effective elastic moduli has been compiled by Watt, *et al.*[31] The review examines the bounding methods used to determine the upper and lower limits on elastic moduli. Upper and lower bounds are used because the exact values of the moduli are never physically realizable. Elastic properties of two-phase materials must have upper and lower bounds. Hashin and Shtrikman[14] utilized a variational method of determining the upper and lower bounds on bulk and shear moduli independent of the geometry of the inclusion. Their development was based on knowing the elastic moduli of the inclusion and the surrounding matrix material and the relative volume fraction of inclusion to matrix material. This bound is quite general so to make approximations of the actual effective bulk and shear moduli, other theories have been developed and are described in the following paragraphs.

The Kuster and Toksöz theory[18] was developed for spherical inclusions and is described in the following manner. If an infinite elastic matrix is composed of material 1 and small spherical inclusions of material 2 are embedded in it, then a larger 'effective' sphere can be defined with effective material properties such that the scattered field from the individual spheres measured at a point in the far field is equivalent to the scattering from the effective sphere.

A second method called 'self-consistent' was derived separately by Budiansky[7] and Hill[16] and is described as follows: if the surrounding matrix is composed of the effective material and the inclusions are composed of aggregations of materials 1 and 2 (each inclusion is homogeneous), then the elastic constants can be found such that the total scattering from material 1 and 2 inclusions vanishes. The self-consistent approach is an impedance matching theory such that when the impedances are matched, the inclusions are transparent to the incoming acoustic wave (i.e. scattering coefficients vanish).[6]

There are other effective medium theories which have been developed but the standard theories are the Kuster-Toksöz (KT) and self-consistent (SC) ones. KT provides a direct

formula for computing the elastic moduli whereas the SC method is more involved because iteration is required to obtain the effective moduli. There are criticisms to both models as discussed by Berryman.[6] However, because of the intuitive results provided by KT, their method of development is chosen in this thesis.

Watt *et al.* also give results for various geometries of inclusions. The geometry is important because it determines the difficulty of evaluating boundary conditions. The reason for this is because effective properties are derived from scattering theory. In Chap. 2 scattering from a cylindrical inclusion was discussed. The displacement field depends on the boundary conditions at the surface of the inclusion. The coefficients which are calculated from the boundary conditions (A_n's, B_n's, etc) are the basis of the effective medium theory. Much work has been done on effective moduli of spheres because of the symmetry of the problem.

This chapter will be devoted to developing analytical solutions for effective elastic moduli where it is assumed that the acoustic wavelength is long compared to the size of the inclusion ($ka \ll 1$). The long wavelength approximation ensures that the material properties will be averaged over. The effective moduli theory assumes materials of the solid and inclusion are homogeneous. Lastly, the theory assumes that multiple scattering does not occur. The theory is based on summing up the contributions from the individual scatterers to arrive at the total field at some point in the far field.

3.2 Long wavelength propagation

As stated before, wave propagation in which the wavelength of the sound wave is long compared to the size of the inclusion is of interest so that any fluctuations in elastic properties will be averaged out. It is assumed that the total displacement field is due to the sum of the scattered fields from the individual scatterers. The elastic matrix is assumed to be homogeneous in which fluid-filled cylindrical inclusions are embedded. The total displacement field in the radial direction measured at a point x is:

$$u(x) = u_{inc}(x) + \sum_{n=1}^{N} u_n(x, x_n) \tag{3.1}$$

where $u(x)$ is the total displacement field, $u_n(x, x_n)$ is the displacement at x due to the wave scattered from the n^{th} cylindrical inclusion and $u_{inc}(x)$ is the displacement at x due

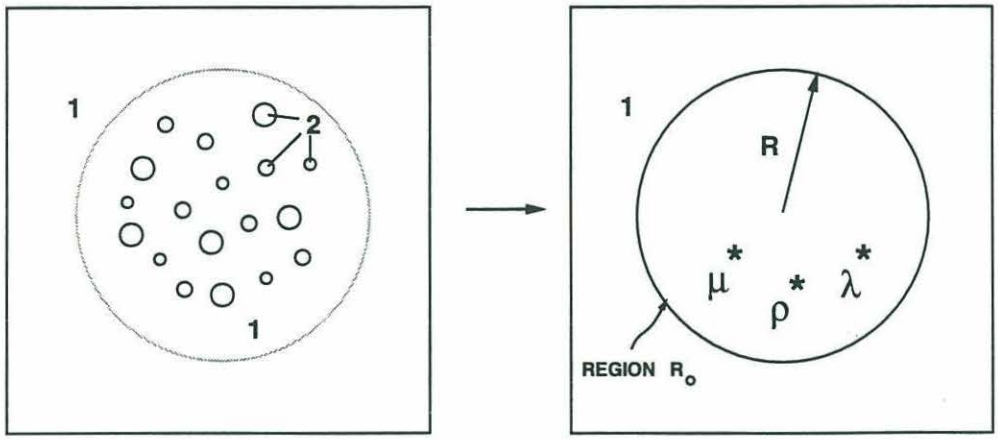

Figure 3-1: Concept of the effective medium theory. Left: elastic matrix of type 1 material with cylindrical inclusions of varying radii of type 2 material. Right: an effective area R_o with effective elastic moduli embedded in type 1 material.

to the incident wave. Now consider the same elastic matrix which has a region R_o in which the fluid inclusions are embedded. An effective medium can be defined which is confined to area R_o with properties such that when the same acoustic wave is incident on it, the displacement at point x is the same as the scattered field generated by the N cylindrical inclusions. Figure 3-1 visualizes this concept of a region R_o with effective moduli. This can be written this as:

$$u(x) = u_{inc}(x) + u^*(x, x_o). \tag{3.2}$$

Equating Eqs. (3.1) and (3.2) yields

$$u^*(x, x_o) = \sum_{n=1}^{N} u_n(x, x_n). \tag{3.3}$$

$u^*(x, x_o)$ is the scattered displacement field from the region R_o having effective elastic properties.

In Sec. 2.4.1 the scattered displacement field was expressed as an infinite series of Hankel functions of the first kind weighted by scattering coefficients computed from boundary conditions at the surface of the cylinder ($r = a$). In order to solve for the effective displacement, the infinite sum must be expanded. The first three terms (A_o, A_1, and A_2) are the major contributors to the scattered field if the following assumption is made: the wavelength of the incident acoustic wave is much longer than the size of the cylindrical inclusion

(i.e $ka \ll 1$). Making this assumption and dropping the exponential time dependence, both sides of Eq. (3.3) can be simplified. Assuming the observation point x is distant ($kr \gg 1$), the left hand side of Eq. (3.3) becomes:

$$u^*(x,x_o) = \sqrt{\frac{2}{\pi k_{p_1} r}} e^{ik_{p_1} r} e^{-i3\pi/4} \{-A_o^* k_{p_1} - A_1^*(1-ik_{p_1})\cos(\theta) + A_2^*(k_{p_1}+2i)\cos(2\theta)\} \quad (3.4)$$

and

$$\sum_{n=1}^{N} u(x,x_n) = \sqrt{\frac{2}{\pi k_{p_1} r}} e^{ik_{p_1} r} e^{-i3\pi/4} \sum_{n=1}^{N} \{-A_{o_n} k_{p_1} - A_{1_n}(1-ik_{p_1})\cos(\theta) + A_{2_n}(k_{p_1}+2i)\cos(2\theta)\}. \quad (3.5)$$

The A_n's are derived directly from the boundary conditions by solving the 3x3 matrix of equations. To solve for A^*, the original equations for solid-solid scattering must be used. The reason for this is that since the scattering is from cylindrical inclusions, no shear wave is supported inside the inclusion ($\mu = 0$). However, for the effective medium theory, there is an effective shear modulus (μ^*) because the surrounding matrix is a solid. This μ^* is not the same as the shear modulus of the solid matrix surrounding the inclusions as will be shown. Appendix A shows the derivation of the scattering coefficients for a solid matrix, solid inclusion. The results of this derivation are used in App. B where the first three terms of the effective scattering coefficient A^* are derived for a scattered compressional wave.

Referring back to Eqs. (3.4) and (3.5), the following constants are defined:

$$A_o^* = \frac{\pi}{4} i k_{p_1}^2 R^2 \left(\frac{\lambda_1 - \lambda^* + \mu_1 - \mu^*}{\lambda^* + \mu_1 + \mu^*}\right) \qquad \tilde{A}_o^* = \frac{\lambda_1 - \lambda^* + \mu_1 - \mu^*}{\lambda^* + \mu_1 + \mu^*}$$

$$A_1^* = \frac{\pi}{4} k_{p_1}^2 R^2 \left(\frac{\rho_1 - \rho^*}{\rho_1}\right) \qquad \tilde{A}_1^* = \frac{\rho_1 - \rho^*}{\rho_1}$$

$$A_2^* = \frac{\pi}{4} i k_{p_1}^2 R^2 \left(\frac{2\mu_1(\mu^* - \mu_1)}{(\lambda_1 + 2\mu_1)(\mu^* + \mu_1) + \mu_1\mu^* - \mu_1^2}\right) \qquad \tilde{A}_2^* = \frac{2\mu_1(\mu^* - \mu_1)}{(\lambda_1 + 2\mu_1)(\mu^* + \mu_1) + \mu_1\mu^* - \mu_1^2}$$

$$A_{o_n} = \frac{\pi}{4} i k_{p_1}^2 a_n^2 \left(\frac{\lambda_1 - \lambda_2 + \mu_1}{\lambda_2 + \mu_1}\right) \qquad \tilde{A}_o = \frac{\lambda_1 - \lambda_2 + \mu_1}{\lambda_2 + \mu_1}$$

$$A_{1_n} = \frac{\pi}{4} k_{p_1}^2 a_n^2 \left(\frac{\rho_1 - \rho_2}{\rho_1}\right) \qquad \tilde{A}_1 = \frac{\rho_1 - \rho_2}{\rho_1}$$

$$A_{2_n} = \frac{\pi}{4} i k_{p_1}^2 a_n^2 \left(\frac{-2\mu_1}{\lambda_1 + \mu_1}\right) \qquad \tilde{A}_2 = \frac{-2\mu_1}{\lambda_1 + \mu_1}.$$

Making these substitutions into Eqs. (3.4) and (3.5) yields:

$$u^*(x,x_o) = \sqrt{\frac{\pi}{8k_{p_1}r}}k_{p_1}^2 R^2 e^{ik_{p_1}r}e^{-i3\pi/4}\left\{-ik_{p_1}\tilde{A}_o^* - \tilde{A}_1^*(1-ik_{p_1})\cos(\theta) + i\tilde{A}_2^*(k_{p_1}+2i)\cos(2\theta)\right\} \quad (3.6)$$

$$\sum_{n=1}^{N} u(x,x_n) = \sqrt{\frac{\pi}{8k_{p_1}r}}k_{p_1}^2 e^{ik_{p_1}r}e^{-i3\pi/4}\sum_{n=1}^{N} a_n^2\left\{-ik_{p_1}\tilde{A}_o - \tilde{A}_1(1-ik_{p_1})\cos(\theta) + i\tilde{A}_2(k_{p_1}+2i)\cos(2\theta)\right\} \quad (3.7)$$

Equating Eqs. (3.6) and (3.7) results in the simplified forms:

$$\tilde{A}_o^* = c\tilde{A}_o \quad (3.8)$$

$$\tilde{A}_1^* = c\tilde{A}_1 \quad (3.9)$$

$$\tilde{A}_2^* = c\tilde{A}_2. \quad (3.10)$$

c is the concentration per unit area of cylindrical inclusions given by:

$$c = \sum_{n=1}^{N} \frac{a_n^2}{R^2}$$

where R is the radius of the effective cylindrical region R_o and a_n's are the individual radii of the N cylindrical inclusions. Equations (3.8) - (3.10) can be easily solved for the effective Lamé parameters and effective density

$$\rho^* = \rho_1 + c(\rho_2 - \rho_1) \quad (3.11)$$

$$\mu^* = \frac{2\mu_1^2 + Q_2(\lambda_1\mu_1 + \mu_1^2)}{2\mu_1 - Q_2(\lambda_1 + 3\mu_1)} \quad (3.12)$$

$$\lambda^* = \frac{\lambda_1 + \mu_1(1-Q_1)}{1+Q_1} - \mu^* \quad (3.13)$$

where Q_1 and Q_2 are constants given by:

$$Q_1 = c\left(\frac{\lambda_1 - \lambda_2 + \mu_1}{\lambda_2 + \mu_1}\right) \quad (3.14)$$

$$Q_2 = c\left(\frac{-2\mu_1}{\lambda_1 + \mu_1}\right). \tag{3.15}$$

When the concentration c is zero, the effective moduli λ^*, μ^*, and ρ^* reduce to the moduli for medium 1. Similarly, when c is 1.0, the effective moduli are the moduli for medium 2.

Having solved for the effective elastic constants and density, the effective wave speeds can be computed using the following relations:

$$C_p^* = \sqrt{\frac{\lambda^* + 2\mu^*}{\rho^*}} \tag{3.16}$$

$$C_s^* = \sqrt{\frac{\mu^*}{\rho^*}}. \tag{3.17}$$

3.3 Bounds on elastic moduli

The derivation of effective moduli in the previous section was based on cylindrical fluid inclusions embedded in an elastic matrix. As stated previously, Hashin and Shtrikman derived upper and lower bounds on effective bulk (K^*) and shear (μ^*) moduli for a two-phase aggregate (1 = solid, 2 = fluid). The bounds for the solid are: [31]

$$K_1^* = K_1 + \frac{\nu_2}{(K_2 - K_1)^{-1} + \nu_1(K_1 + \frac{4}{3}\mu_1)^{-1}} \tag{3.18}$$

$$\mu_1^* = \mu_1 + \frac{\nu_2}{(\mu_2 - \mu_1)^{-1} + 2\nu_1(K_1 + 2\mu_1)(5\mu_1(K_1 + \frac{4}{3}\mu_1))^{-1}}. \tag{3.19}$$

The Eqs. (3.18) and (3.19) are the bounds for the solid matrix where ν is the fraction of material present. To obtain the bounds for the fluid, the subscripts 1 and 2 need to be interchanged. As a side note, the bulk modulus K can be written in terms of Lamé parameter λ and shear modulus μ as:

$$K = \lambda + \frac{2}{3}\mu. \tag{3.20}$$

Walpole [30] utilizes the self-consistent approximation to derive the bounds for "needle-shaped" inclusions. The needle shape is similar to the derivation in this thesis for a cylinder in which the radius (a) of the cylinder is negligible compared to its length (l). The needle

shape is arrived at by letting the radius a vanish. Watt [31] simplifies Walpole's original expressions for effective moduli to obtain

$$\frac{K^* - K_1}{K_2 - K_1} = \nu_2 \left(1 + \nu_1 \frac{K_2 - K_1}{K_1 + F_k}\right)^{-1} \tag{3.21}$$

where

$$F_k = \frac{1}{3}\mu_1 + \mu^* \tag{3.22}$$

and

$$\frac{\mu^* - \mu_1}{\mu_2 - \mu_1} = \nu_2 \left(1 + \nu_1 \frac{\mu_2 - \mu_1}{\mu_1 + F_\mu}\right)^{-1} \tag{3.23}$$

$$F_\mu = \left\{5\left[\frac{1}{3(K_1 + \frac{1}{3}\mu_1 + \mu^*)} + \frac{2(2\mu_1 + \mu^* + g)}{(\mu_1 + \mu^*)(\mu_1 + g)}\right]^{-1}\right\} - \mu_1 \tag{3.24}$$

$$g = \frac{\mu^*(K^* + \frac{1}{3}\mu^*)}{K^* + \frac{7}{3}\mu^*}. \tag{3.25}$$

The subscript 1 denotes the needle phase and 2 is the phase of the elastic material. Once again, $\nu_{1,2}$ is the fraction of phase 1 or 2 present. As a check, the effective moduli for cylindrical inclusions were compared against the Hashin-Shtrikman bounds and the self-consistent needle formulation. The results are plotted in Fig. 3-2. The solid line represents the normalized effective bulk and shear moduli which are derived for a composite of cylinders embedded in an elastic medium. The dashed line represents effective moduli for the self-consistent scheme for fluid-filled needle inclusions (SCS needle) in a solid matrix. The last two curves represent the upper and lower HS bounds for an aggregate of fluid spheres in an elastic matrix. The fluid is considered water with wave speed of 1490 m/s and density 1000 kg/m^3. The solid is polypropylene with $C_p = 2528$ m/s, $C_s = 1270$ m/s, and density 913 kg/m^3. The Lamé parameters were computed using Eqs. (2.5) and (2.6). The bulk modulus was then calculated using Eq. (3.20). The effective moduli have been normalized by their bulk and shear moduli for polypropylene. We see that the SCS needle moduli lie between the HS bounds. The HS lower bound for the shear modulus is zero since the inclusions are fluid ($\mu = 0$). Also note that the self-consistent shear modulus vanishes at a concentration of 55% for needles. This critical fraction is calculated using

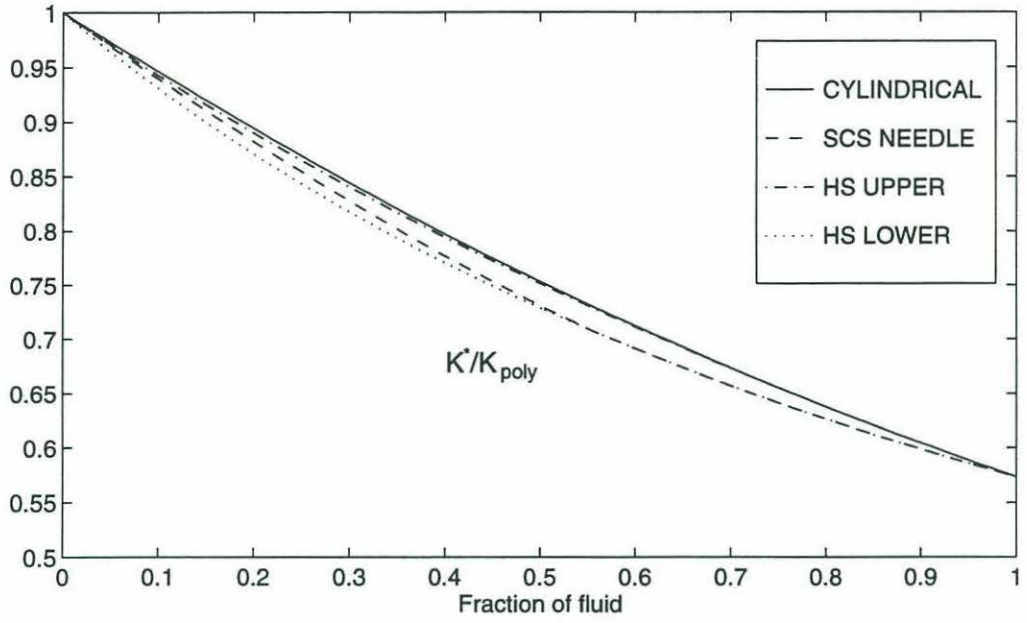

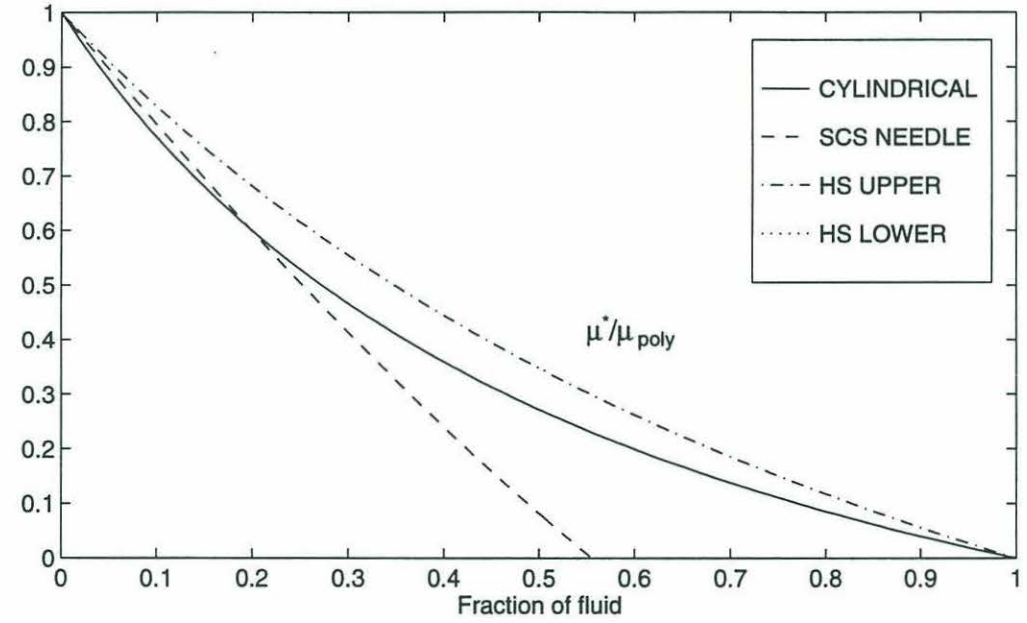

Figure 3-2: Comparison of bounds on effective moduli. Bounds have been normalized by the moduli of polypropylene. Top: effective bulk modulus for cylinders (–), self-consistent scheme for needles (- -), Hashin-Shtrikman (HS) upper bound (-.-) and HS lower bound (...). Lower: effective shear modulus using same schemes as above.

Eqs. (3.23) - (3.25). The effective bulk modulus (K^*) for the cylinder is outside the HS upper bound for concentrations of inclusions less than 60%. Although, this may appear to be a problem with the theory developed in this study, it is not since the Hashin-Shtrikman bounds are *general* bounds, independent of geometry. Most importantly, note that this formulation is qualitatively consistent with the HS and self-consistent needle formulations.

Chapter 4

Single Scattering Experiment

This chapter describes the laboratory experiment for scattering from a single fluid inclusion. Calibration is performed to determine the compressional wave speed and attenuation for solid polypropylene. It was found that attenuation is linearly dependent on frequency as predicted. Experimental work is performed for a single fluid inclusion embedded in the attenuating polypropylene. Scattering vs. angle measurements are made every 20° for ka values of 1.9, 2.4, 8.8, and 11.0. The experimental results of the total displacement field are compared with theoretical predictions.

4.1 Overview

Experimental data was first presented for scattering vs. angle from cylindrical discontinuities in a solid by White [33]. He compared experimental work to theoretical developments for cavities and mercury filled bores. Other investigators have studied scattering of sound by solid cylinders in elastic media [3, 5] as well as scattering by solid cylinders in fluid media [10, 20]. Kim, *et al.* measured sound scattering from cylindrical cavities in attenuating and non-attenuating media [17]. Although White measured scattering from a mercury filled bore, he did not account for attenuation in his theoretical comparisons. In this study, water is used as the fluid in the inclusion. This will produce different results acoustically due to the impedance contrast (ρc) at the boundary of the cylinder. This work is complimentary to the work of others but it is necessary as a prelude for the experimental validation of the effective medium concept derived in Chap. 3.

4.2 Experimental Setup

The experimental setup is shown in Fig. 4-1. Measurements were made separately for scattering vs. angle for 3/8 and 7/4 inch diameter cylindrical bores in a 12 inch diameter polypropylene rod. Facets were machined at angular increments of 20° to ensure proper contact between the transducer face and polypropylene. Polypropylene was chosen as the material of interest because its wave speed and density are similar to that of ice [12]. Ice has an average compressional wave speed (C_p) of 3600 m/s, shear wave speed (C_s) of 1700 m/s and density (ρ) of 910 kg/m^3. The corresponding values for polypropylene are $C_p = 2528$ m/s, $C_s = 1270$ m/s and $\rho = 913$ kg/m^3. The compressional wave speed was determined experimentally and the shear wave speed taken from the results by Hartmann and Jarzynski [13] at 600 kHz.

The experiment described herein was performed in a freshwater tank. The decision to immerse the apparatus in the tank was made to ensure that proper coupling existed between the transducers and the polypropylene. Additionally, the filling of the bores by the water was accomplished by immersion. The sound sources are plane circular transducers manufactured by Radarsonics, Inc. operating at 160 kHz and 200 kHz. The receivers (transceivers) are identical to the transmitters. The source and receiver were positioned on the facets and held in place by an aluminum support ring. Brass nuts on the transmitter and receiver were hand tightened against the aluminum ring such that they applied equal and opposite forces against the polypropylene. A rubber insulating washer was placed between the brass nut and aluminum ring to prevent any coupling between the transducer and aluminum support ring. For the scattering vs. angle experiments, the transmitter remained on the same facet and the receiver was moved to other facets in 20° increments. In this case, dummy transducers were placed opposite the source and receivers to ensure equal distribution of force to keep the transducers in place.

Calibration consisted of measuring the received signal in the tank of water without the polypropylene present. The transducers were separated by a distance of 97 cm. The compressional wave speed measured in freshwater was 1430 m/s. The next calibration was done on the solid polypropylene rod at 160 kHz and 200 kHz to determine attenuation and compressional wave speed. A sampling frequency of 10 MHz on the oscilloscope was used because of the need for accurate time resolution for the effective medium experiments.

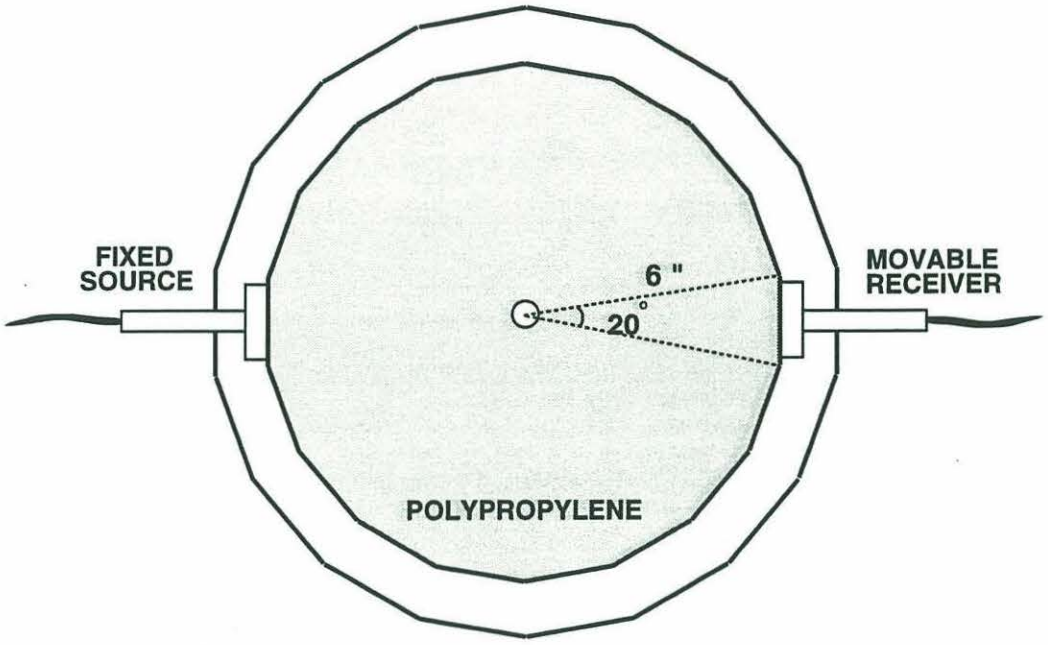

Figure 4-1: Geometry for scattering experiment of a single water-filled cylindrical inclusion in polypropylene. Aluminum support ring aligns the transducers.

4.3 Angular Scattered Displacement Field

A scattering experiment from a single cylindrical inclusion was performed on a 3/8 inch diameter fluid-filled inclusion. For a compressional wave speed (C_p) of 2528 m/s, the ka value at 160 kHz is 1.89 and at 200 kHz, ka = 2.37. Four separate experiments were conducted at each frequency. The experiment was conducted as follows: The source was placed in direct contact with one of the facets on the polypropylene.[1] The receiver was placed directly opposite the transmitter on the other facet at 0°. A pulse (gate) was generated by a pulse generator (Hewlett Packard (HP) 8011A) and sent to a function generator (HP 8116A) which generated a gated sinusoidal signal. The resulting gated sine wave of 30 cycles was sent to a power amplifier (200 watt ENI, Inc. 2100L) where it was then transmitted. The received signal was sent to a pre-amplifier (47 dB gain) made at WHOI and then bandpass filtered by a RITEC (BR-640) broadband receiver with low and high cutoff frequencies of 50 kHz and 3 MHz respectively. The filtered signal was then sent to a digital oscilloscope (Tektronix 2230). Each ping was averaged 8 times and 4096 points of the signal transferred from the oscilloscope to a personal computer via GPIB interface.

[1] on subsequent experiments, the facet on which the source was placed remained the same

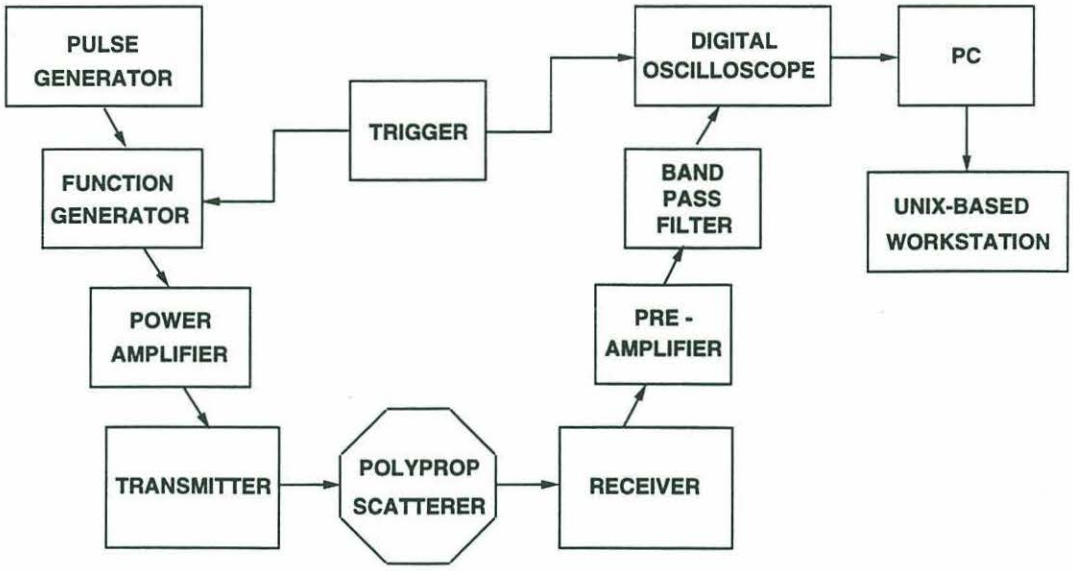

Figure 4-2: Block diagram showing experimental setup and flow of data.

Data from the personal computer was transferred to a Unix-based workstation where the data analysis was performed. Figure 4-2 shows graphically the flow of information. The Power Spectral Density (PSD) of each run was computed to determine a measure of the energy at each frequency. The PSD value was computed using a Fast Fourier Transform (FFT) length of 2048 points for each run. The value of the PSD at the frequency of interest (160 kHz or 200 kHz) was recorded for each angle and stored for future use.

The results of the experiment vs. theoretical predictions for scattering from the 3/8 inch diameter hole at 160 and 200 kHz are shown in Figs. 4-3 and 4-4 respectively. The experimental results for the total displacement, plotted as symbols in the figures, are shown for four different runs. To obtain the displacement from the PSD (which is a measure of energy), the square root of the PSD is calculated at the frequency of interest. This is justified since the transmitted wave is narrowband. The PSD for a narrowband or monochromatic source is proportional to U_o^2 where U_o is the amplitude of the displacement. Hence the square root of the PSD will be proportional to the displacement U_o. The average of the experimental results at each angle are also shown in the figures. The solid line is the theoretical prediction of the total displacement field.

The experimental results are scaled by a factor such that the experimental and theoretical values agree at a scattering angle of zero degrees (forward scatter direction). A scaling

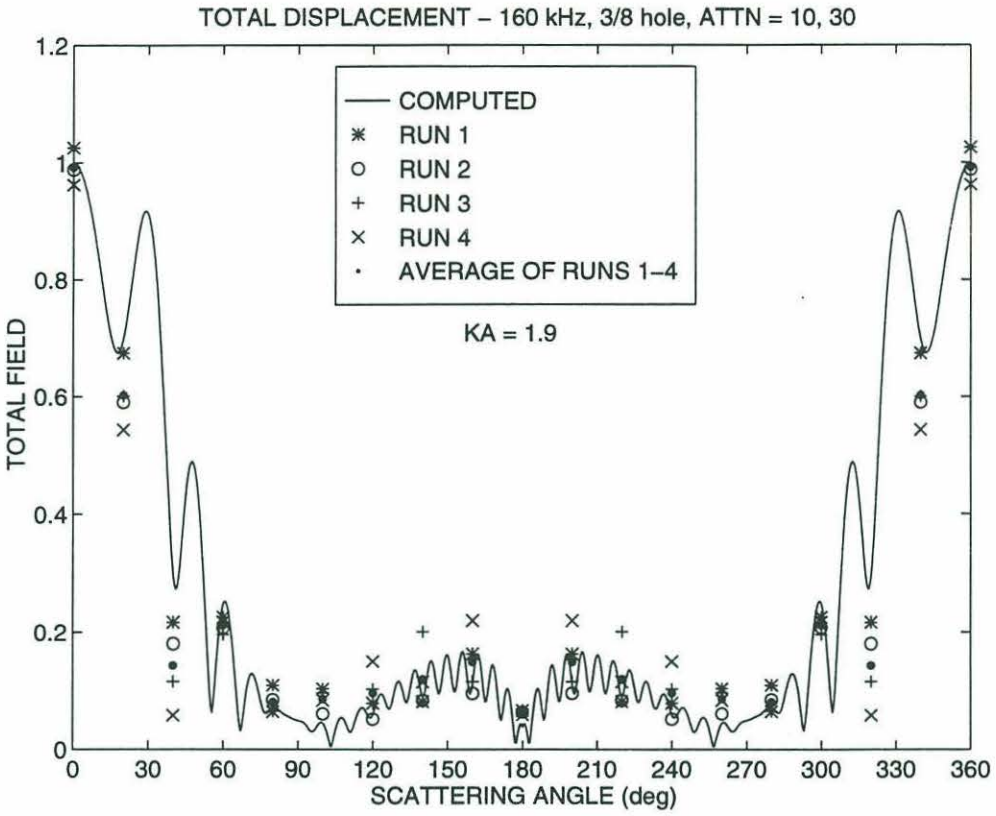

Figure 4-3: Total displacement field as a function of angle for 3/8" diameter fluid inclusion measured at 160 kHz. Solid line represents the numerical prediction and the symbols the experimental data.

factor of 0.95 is used on the experimental data for the 3/8 inch, 160 kHz case and a factor of 0.7 is used at 200 kHz. Figures 4-5 and 4-6 show the results for scattering from a 7/4 inch diameter hole at 160 and 200 kHz. The results at 160 kHz are scaled by a factor of 1.4 and 2.8 at 200 kHz. As can be seen, qualitatively the results fit well with the theoretical predictions. The total field as predicted by the theory was computed using $C_p = 2528$ m/s, $C_s = 1270$ m/s, $\alpha_p = 10$ Neper/m @ 160 kHz and 12.5 Neper/m @ 200 kHz, and $\alpha_s = 30$ Neper/m @ 160 kHz and 36 Neper/m @ 200 kHz. The value for compressional attenuation (α_p) was computed from the measured experimental data with solid polypropylene. In the absence of inhomogeneities, the pressure of an acoustic wave in a solid experiences a 1/r spherical spreading loss as well as exponential decay due to attenuation. Similarly in water, there is a 1/r spreading loss but no attenuation over short distances. Mathematically we can write this as:

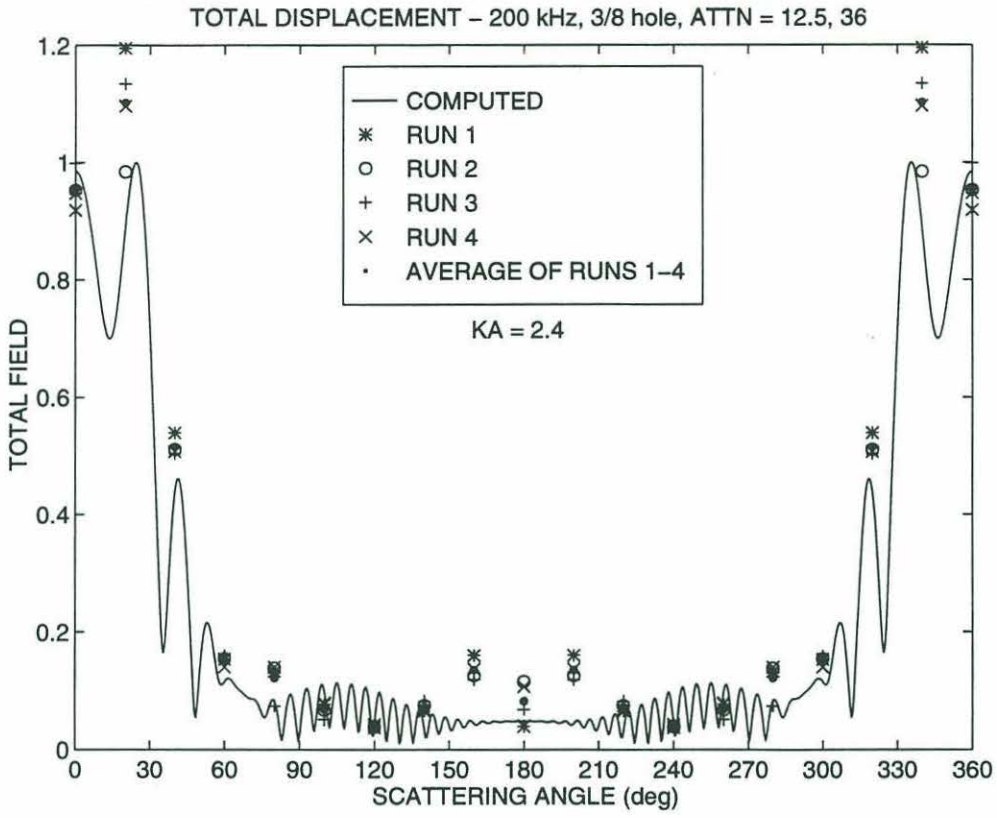

Figure 4-4: Total displacement field as a function of angle for 3/8" diameter fluid inclusion measured at 200 kHz. Solid line represents the numerical prediction and the symbols the experimental data.

$$\mathrm{P}_1 \propto \frac{1}{r_1} e^{-\alpha_1 r_1} \quad \text{elastic} \tag{4.1}$$

$$\mathrm{P}_2 \propto \frac{1}{r_2} \quad \text{water.} \tag{4.2}$$

Taking the ratio of Eqs. (4.1) and (4.2) and solving for the attenuation α_1 in Neper/m yields:

$$\alpha_1 = -\frac{1}{r_1} \ln \frac{\mathrm{P}_1 r_1}{\mathrm{P}_2 r_2} \tag{4.3}$$

where $r_{1,2}$ are the ranges between the source and receiver and $\mathrm{P}_{1,2}$ are the received pressure levels in the solid and water respectively. The values of compressional attenuation determined experimentally are 10.0 Neper/m and 12.5 Neper/m for 160 kHz and 200 kHz respectively. This confirms that compressional wave attenuation is linearly dependent on fre-

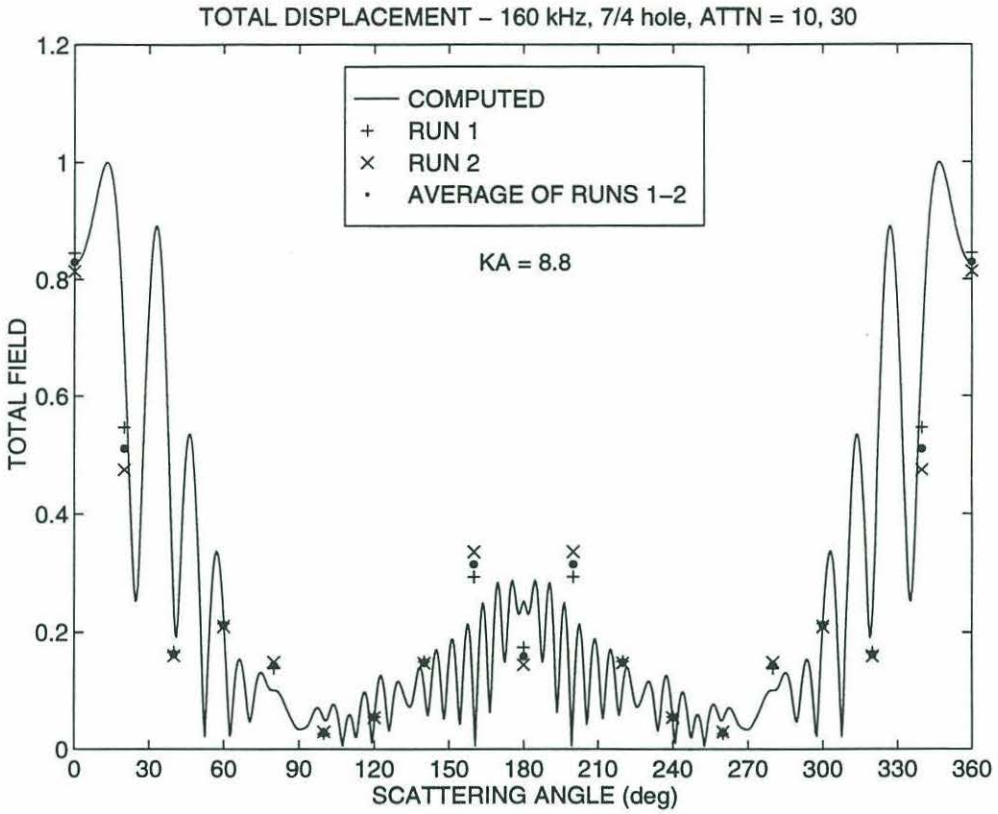

Figure 4-5: Total displacement field as a function of angle for 7/4" diameter fluid inclusion measured at 160 kHz. Solid line represents the numerical prediction and the symbols the experimental data.

quency. The value of shear wave attenuation (α_s) was chosen to be three times greater than the compressional wave attenuation (α_p) since it could not be measured experimentally. Work done by McCammon and McDaniel [22] found a value of $\alpha_s \sim 3$ x greater than α_p in sea ice. Although polypropylene and sea ice are not the same, they both possess crystalline microstructure. Without any shear wave attenuation information, values are chosen as three times that of compressional wave attenuation.

The original development assumed a plane wave incident on a cylinder. Since this was chosen for mathematical ease, a correction to the theoretical prediction must made to account for spherical spreading of the wave and beam patterns of the transmitter and receiver. Figure 4-7 outlines the geometry of the corrections. Ψ is the half-power beamwidth of the source and d is the diameter of the ceramic within the source. The distance from the center of the inclusion to the transmitter and receiver is denoted by r. R is the distance from the transmitter to receiver and R' is the distance from point O to the receiver. The

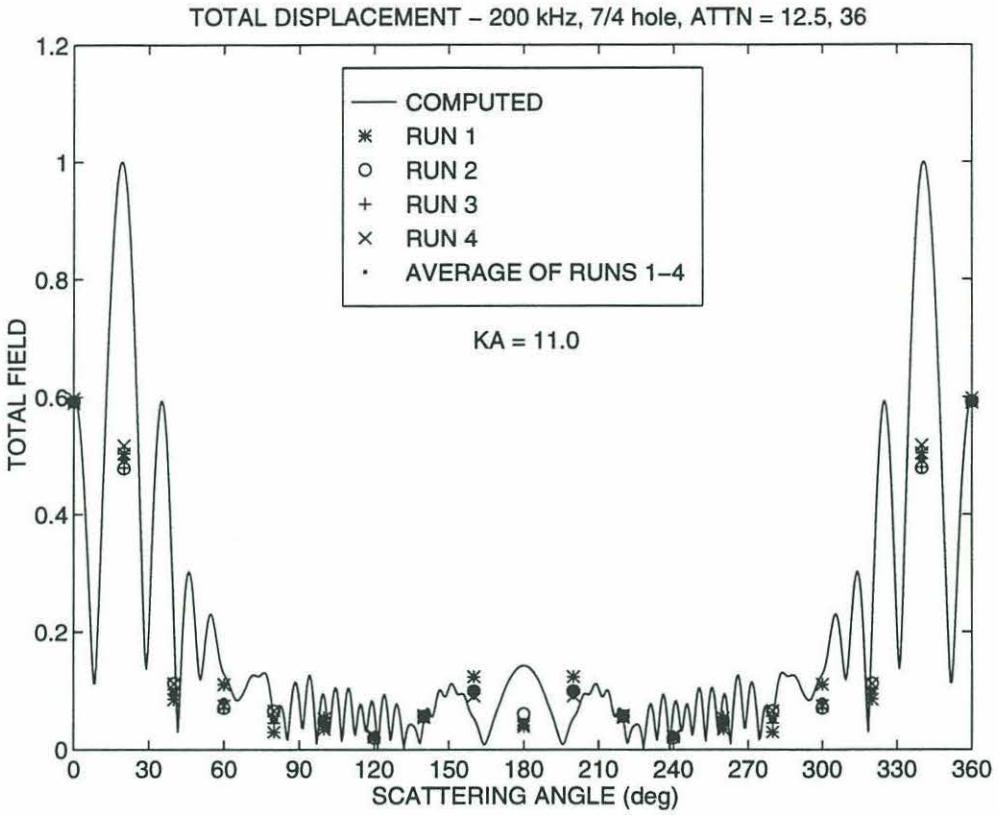

Figure 4-6: Total displacement field as a function of angle for 7/4" diameter fluid inclusion measured at 200 kHz. Solid line represents the numerical prediction and the symbols the experimental data.

point O is defined as a fictitious point where a point source located here will generate a wave in phase at the transmitter (neglecting the small curvature of the wave at either end of the transducer ceramic). The distance r_o, as measured from point O, is computed from the half-power beamwidth of the source. The potential at the receiver incident from point O is:

$$\Phi_{inc} = \frac{r_o}{R'} e^{ikR}. \tag{4.4}$$

The amplitude r_o/R' accounts for spherical spreading of the wave and the exponential term (ikR) represents the change in phase from transmitter to receiver. The actual values of R and R' from the geometry of the problem are given in Eqs. (4.5) and (4.6).

$$R = 2r\cos\left(\frac{\theta}{2}\right) \tag{4.5}$$

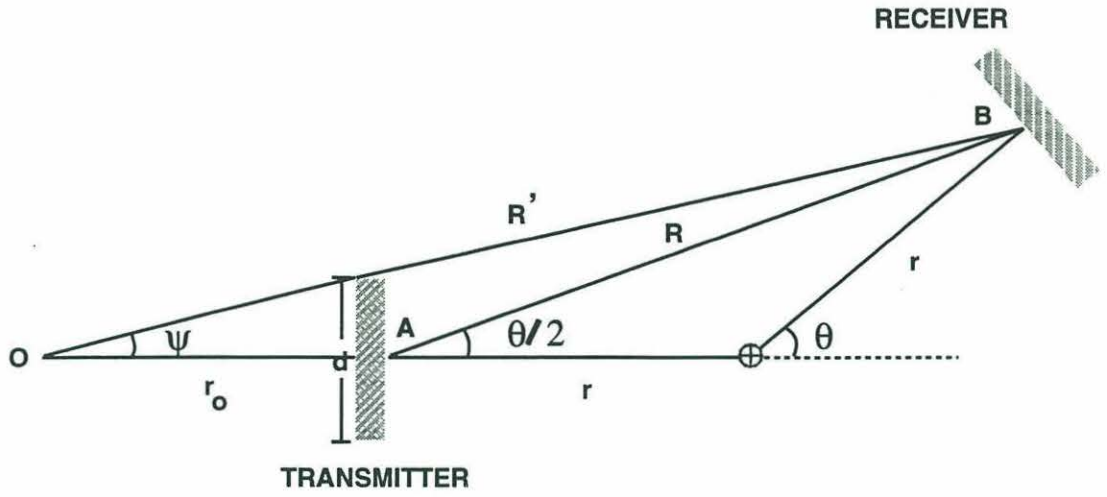

Figure 4-7: Geometry showing the correction needed to the theoretical development of plane wave scattering.

$$R' = \sqrt{r_o^2 + 2r(r_o + r)(1 + \cos(\theta))} \tag{4.6}$$

Using the potential derived previously, the incident radial displacement at the receiver is:

$$\tilde{u}_{inc} = \frac{\partial \Phi_{inc}}{\partial r} = r_o \left[\frac{1}{R'} \frac{\partial e^{ikR}}{\partial r} + e^{ikR} \frac{\partial (\frac{1}{R'})}{\partial r} \right] [B_t(\theta) B_s(\theta)]^{1/2} \tag{4.7}$$

where the beam pattern for a circular plane transmitter and receiver is defined to be [29]:

$$B_{t,s}(\theta) = \left[\frac{2J_1(ka \sin\theta)}{ka \sin\theta} \right]^2 . \tag{4.8}$$

Simplifying Eq. (4.7) yields

$$\tilde{u}_{inc} = r_o e^{ikR} \left[\frac{ik2\cos\left(\frac{\theta}{2}\right)}{R'} - \frac{(r_o + 2r)(1 + \cos(\theta))}{R'^3} \right] [B_t(\theta) B_s(\theta)]^{1/2} . \tag{4.9}$$

From inspection of Eq. (4.9) it can be seen that the second term on the right hand side of the equation is negligible compared to the first term. Making this assumption yields the following approximate solution to the incident field:

$$\tilde{u}_{inc} \approx \frac{r_o}{R'} 2ik \cos\left(\frac{\theta}{2}\right) B(\theta) e^{ikR} e^{-ikr} . \tag{4.10}$$

It is assumed $B_t(\theta) = B_s(\theta) = B(\theta)$.

The radial scattered displacement at the receiver is modified to account for attenuation and spherical spreading as given by:

$$\tilde{u}_r^{scatt} = \frac{r_o}{r_o + r} e^{-\alpha_p r} u_r^{scatt}. \tag{4.11}$$

The amplitude term $r_o/(r_o + r)$ accounts for spherical spreading from point O to the center of the inclusion and the exponential term $(-\alpha r)$ accounts for attenuation of the wave as it propagates from the transmitter to the inclusion. The expression for u_r^{scatt} is defined by Eq. (2.38). The total displacement in the radial direction is the sum of the incident and scattered displacements as defined in Eqs. (4.10) and (4.11).

Chapter 5

Effective Medium Experiment

In Chap. 3 the foundation was laid for the theory behind the effective medium concept and a set of equations derived which could be used to compute effective moduli for varying concentrations of cylindrical inclusions embedded in a homogeneous elastic medium. In this chapter, the results are presented from a laboratory experiment which was conducted to validate the effective medium concept for fluid-filled cylindrical inclusions in a polypropylene matrix.

5.1 Overview

A laboratory experiment was conducted with identical conditions to those described in Chap. 4. Calibration was performed on a solid piece of polypropylene to determine the compressional wave speed. After calibration was complete, holes were drilled in the polypropylene to simulate brine channels in the the ice. The polypropylene was immersed in the laboratory tank and the traveltimes measured using a sound source of 160 kHz. Knowing the separation between source and receiver, it is trivial to compute the average wave speed. The wave speeds were measured for different concentrations of inclusions to compare with theoretical predictions.

5.2 Experimental setup

The block diagram shown in Fig. 4-2 shows the experimental setup for both the calibration and experiment. A sound source of 160 kHz was chosen over 200 kHz because the effective medium theory is valid only at low ka. Calibration was performed using a single sinusoidal

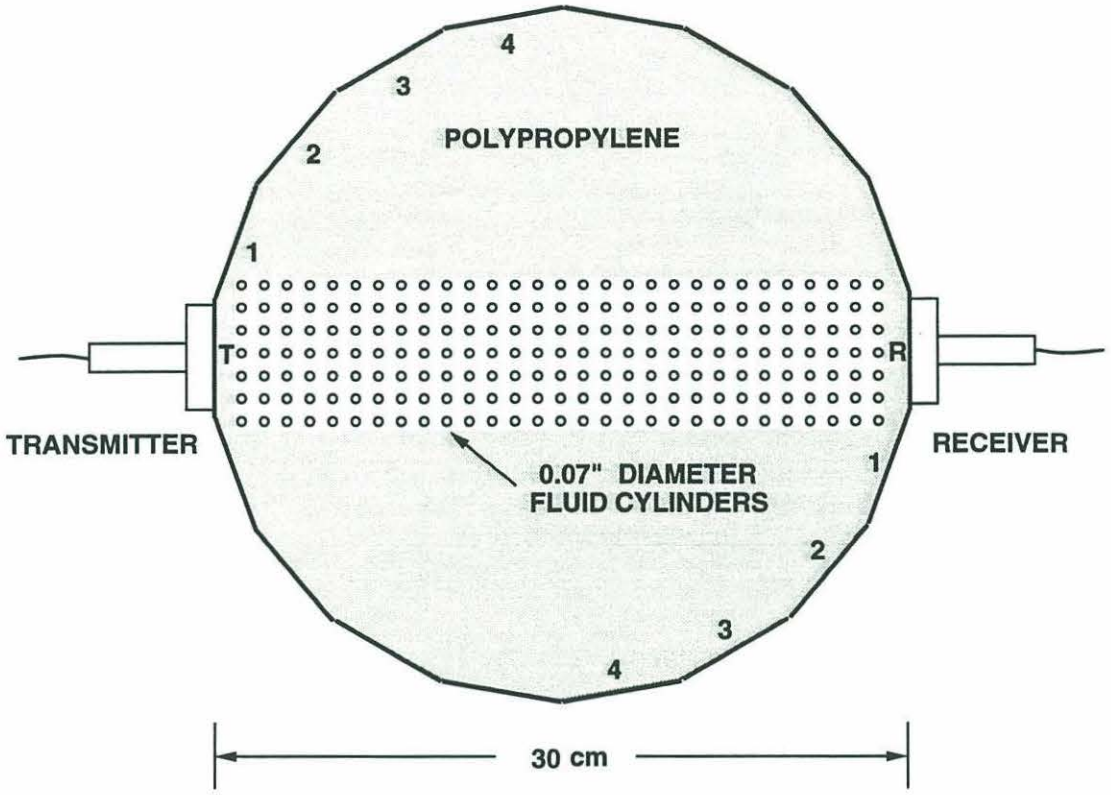

Figure 5-1: Top view of polypropylene with holes drilled to simulate brine channels. The concentration of ensonified holes was varied by positioning the source and receiver at different facet locations 'T-R', '1-1', etc.

pulse to accurately determine the wave speed in the polypropylene. The received signal was averaged over 8 pings, sampled at 10 MHz, digitized and sent from the oscilloscope to a personal computer via GPIB interface. This sampling frequency was chosen to ensure fine enough resolution to determine arrival times of the the direct path signal. The use of a single pulse made it easy to visually pick the arrival time.

To validate the effective medium theory, holes had to be drilled in the polypropylene to simulate cylindrical brine channels in sea ice. 203 holes, 0.07 inches in diameter, equally spaced every 1 cm were drilled in the polypropylene. Figure 5-1 shows a top view of the polypropylene in which the holes were drilled. Figure 5-2 shows a side view of the same setup.

The transmitter and receiver were placed opposite one another on facet '4'. The traveltime was measured for this path and then the source and receiver were moved counterclockwise to the '3-3' position. Moving the transducers in this manner effectively changed

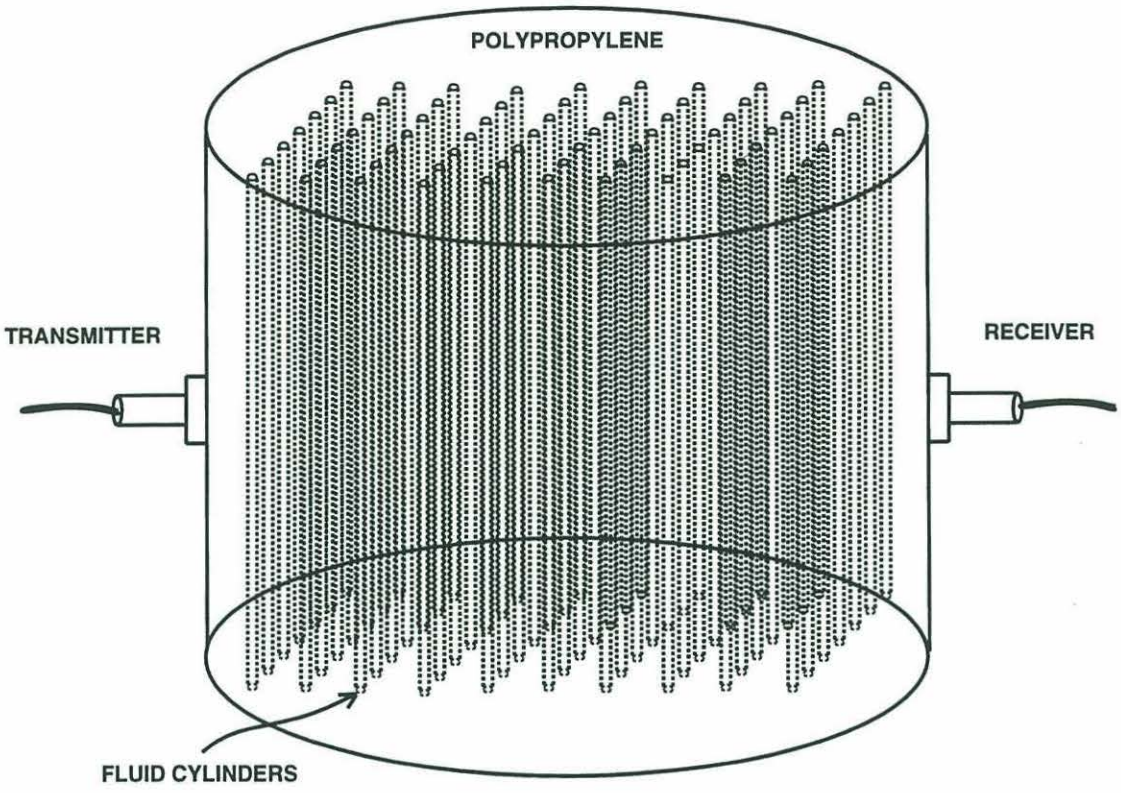

Figure 5-2: Side view of polypropylene showing vertical cylindrical holes.

the concentration of the fluid cylinders without having to drill/fill additional holes. The transmitter has a finite beamwidth so it will ensonify more holes as the transducers are moved from the '4-4' position to the 'T-R' position.

5.3 Experimental Results

Figure 5-3 shows the received signal for the different transducer locations. The top figure is the calibration signal at 160 kHz with no holes with the source and receiver at position 'T-R'. The next figure down shows the received signal for polypropylene with holes for the transducers at position '4-4'. The amplitude has decreased slightly and the arrival time is later than for the no hole case. This trend in reduction of amplitude and increase in delay of arrival time as the transducers are moved from '4-4' to 'T-R' is due to the reduction in the number of fluid cylinders ensonified. Visually this can be seen in the bottom 4 panels of Fig. 5-3.

The arrival times for the five different concentrations of cylinders are listed in table 5.1

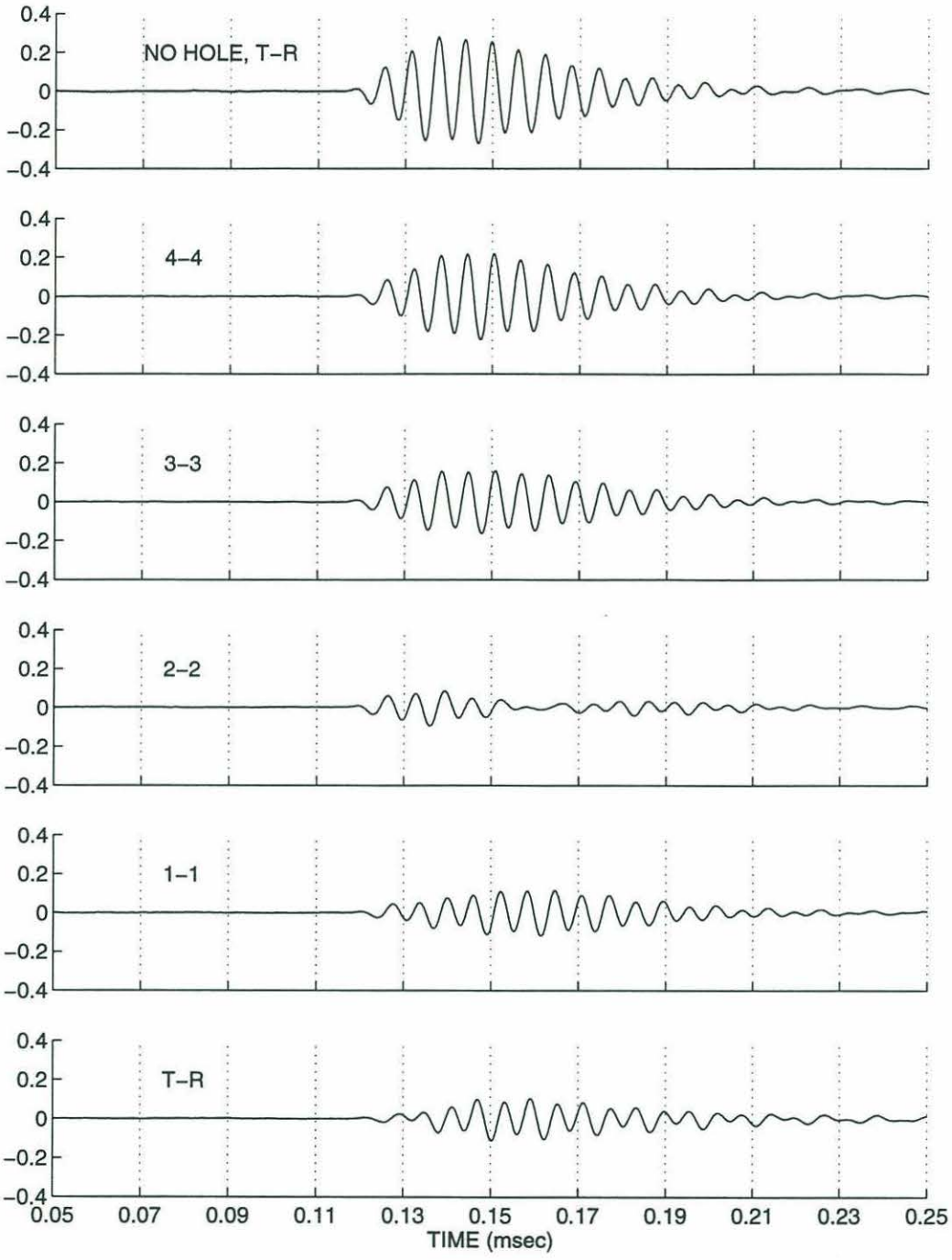

Figure 5-3: Received signal for different source-receiver locations. Top panel is for no hole case. The following panels sequentially show the received signal as the the transducers are moved from facet position 4-4 to T-R. Note the reduction in amplitude and delay in arrival time as the concentration of cylindrical holes increases.

Transducer position	Arrival time (μsec)	Number cylinders	Percent concentration (%)
T-R	121.5	87	2.40
1-1	120.2	60	1.66
2-2	119.6	34	0.94
3-3	119.1	25	0.69
4-4	119.0	23	0.63

Table 5.1: Table of arrival times, the number of fluid cylinders and the percent concentration of fluid cylinders for different source and receiver positions. The ensonified area is 3 cm wide.

for a distance of 30 cm separating the source and receiver. Using this information, the wave speed can be calculated using

$$C_p = \frac{\mathrm{L}}{\Delta t} \tag{5.1}$$

L = distance separating source and receiver

Δt = measured traveltime.

The percent concentration of cylinders is calculated by determining the number of cylinders per area ensonified. The total area ensonified was determined from the transducer crystal diameter. The diameter of the crystal is 1.1 inches (approximately 2.8 cm). To remain conservative, an average rectangular area of 3 cm by 30 cm was determined to be the ensonified area. Table 5.1 lists the number of cylindrical holes which were ensonified as well as the percent concentration. The concentration (c) is calculated by:

$$c = \frac{\text{area of cylinders x number of cylinders ensonified}}{\text{total area ensonified}}$$

where the area of an individual cylinder is $2.48\text{x}10^{-2}$ cm^2 and the total ensonified area is 90 cm^2.

The experimental results for wave speed vs. concentration of fluid cylinders are shown in Fig. 5-4. The theoretical prediction is given by the solid line and was determined from Eq. (3.16). The wave speeds for the no hole case were used as the 0% initial values for the theoretical predictions. The Lamé parameters λ and μ were determined using C_p = 2528 m/s and C_s = 1270 m/s. The results at low concentrations of inclusions matched

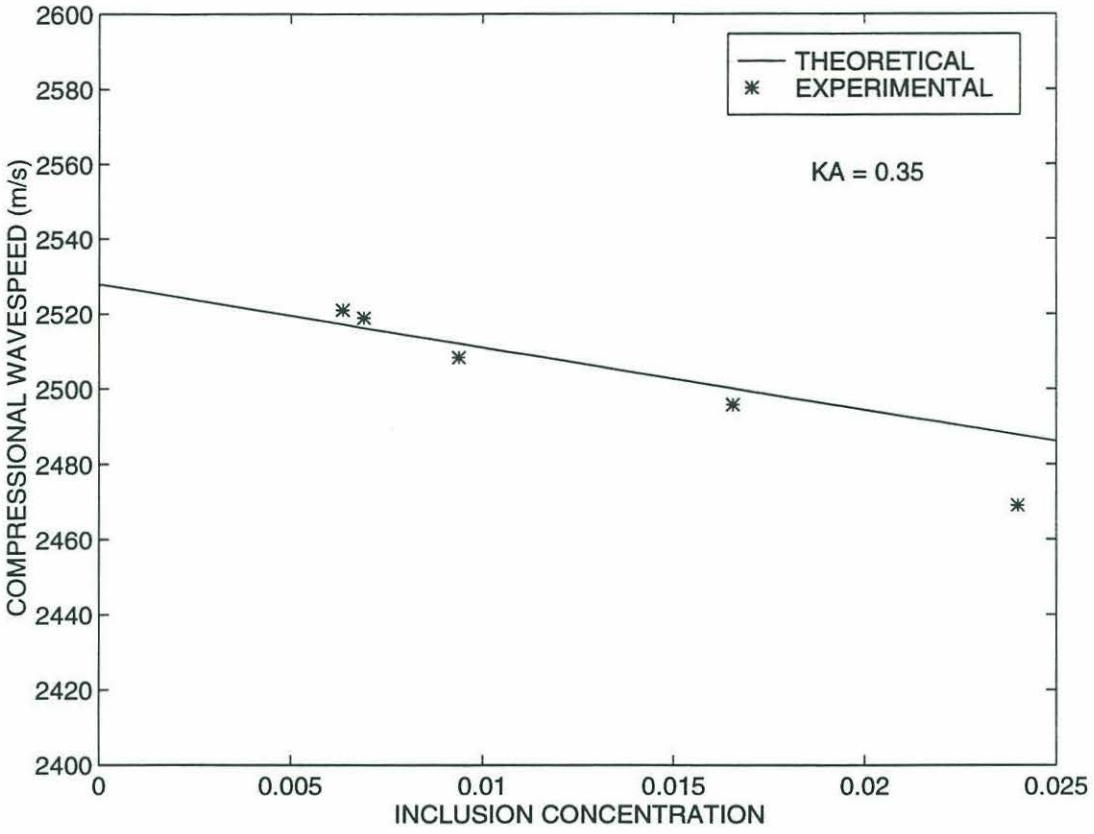

Figure 5-4: Predicted wave speed (solid) and experimental results (*) for varying concentrations of fluid cylinders.

the theoretical predictions very well. However, the experimental result for the highest concentration deviated from the theoretical curve. The discrepancy is possibly due to the breakdown in the effective medium theory because the theory is based on low ka approximations to the Hankel and Bessel functions. It should be noted that this deviation in sound speed is small (approximately 19 m/s or 0.75%). In this experiment, the ka value corresponds to 0.35 at 160 kHz. In actual tomography experiments, ka may be of the order 0.05.

5.4 Comparison of theory with empirical Arctic ice relationships

The theoretical prediction of compressional wave speeds vs. concentration of fluid cylinders was in close agreement with laboratory results. However, the true test of the validity of the

effective medium theory is comparison with field data. Ideally, one would like to grow sea ice without any inhomogeneities to determine baseline compressional and shear wave speeds. One could then use these baseline wave speeds as inputs to the effective medium theory and derive the effective acoustic wave speeds as a function of brine volume content. However, it is impossible to grow sea ice without inhomogeneities. Consequently empirical formulas must be utilized which have been derived from field experiments as well as equations derived from equations of state. These equations can be used to derive zero percent brine volume acoustic wave speeds. These baseline values can then be used in effective medium theory for deriving effective acoustic wave speeds. In this section wave speeds derived from empirical relationships and equations of state are compared with those from effective medium theory. Specifically, Frankenstein and Garner [11] derived a set of equations which relates brine volume content to temperature and salinity of the ice. Langleben and Pounder [19] derived a set of equations which relates Young's modulus of elasticity to brine volume content. These two relations are used to compute the compressional wave speed in the ice vs. brine volume and compare them to theoretical predictions of compressional wave speed.

The equations which Frankenstein and Garner [11] derived were based on equations of state. The brine volume content ν (ppt) is related to temperature T (° C) and salinity S (ppt) by the following relations:

$$\nu = \mathrm{S}\left(\frac{52.56}{|\mathrm{T}|} - 2.28\right), \quad -.5 \geq \mathrm{T} > -2.06\,^{\circ}\mathrm{C} \tag{5.2}$$

$$\nu = \mathrm{S}\left(\frac{45.917}{|\mathrm{T}|} + 0.93\right), \quad -2.06 \geq \mathrm{T} > -8.2\,^{\circ}\mathrm{C} \tag{5.3}$$

$$\nu = \mathrm{S}\left(\frac{43.795}{|\mathrm{T}|} + 1.189\right), \quad -8.2 \geq \mathrm{T} > -22.9\,^{\circ}\mathrm{C}. \tag{5.4}$$

Langleben and Pounder [19] derived an empirical relationship between Young's modulus of elasticity E ($\mathrm{N/m^2}$) and brine volume based on least-squared fits of data from four separate field measurements made in multi-year sea ice. Two separate relationships were derived depending on the season. The equations are listed below:

$$\mathrm{E} = (10.00 - .351\nu)10^9 \quad \text{for cold sea ice} \tag{5.5}$$

$$\mathrm{E} = (8.90 - .163\nu)10^9 \quad \text{for warm sea ice} \tag{5.6}$$

where ν is the brine volume expressed as a percentage. Knowing Young's modulus of elasticity, The compressional and shear wave speeds in the ice can be calculated as follows:

$$C_p = \sqrt{\frac{E}{\rho}\frac{(1-\sigma)}{(1+\sigma)(1-2\sigma)}} \quad \text{(m/s)} \tag{5.7}$$

$$C_s = \sqrt{\frac{E}{\rho}\frac{1}{2(1+\sigma)}} \quad \text{(m/s)}. \tag{5.8}$$

ρ is the density which is taken to be an average 913 kg/m^3 and σ is Poisson's ratio which is assumed to be 0.3.

Two separate plots were generated to compare the theoretical and empirical relations. Figure 5-5 shows the compressional wave speed for the warm (summer) and cold (winter) months. Because the terms cold and warm are ambiguous, cold is defined as an ice temperature of -15°C and warm as a temperature of -5°C. The top panel shows the wave speed as a function of brine volume for the winter months. The empirical (solid) curve is computed using Eqs. (5.4), (5.5), and (5.7) with salinity S varying from 0 to 10 ppt. Using these values the brine volume ranges from 0 to 4 pph (0-4%). The predicted (dashed) curve is the effective wave speed using effective medium theory. The empirical compressional and shear wave speeds for 0% brine volume are used as initial 0% values for the effective medium wave speeds. These initial wave speeds are used to compute the Lamé parameters λ and μ which are used in Eqs. (3.11) - (3.17) to compute effective wave speeds. The difference in wave speeds at 4 pph brine volume is approximately 110 m/s or 3% difference. It is pertinent to note that the empirical relations of Eqs. (5.4) and (5.5) are based on field measurements. The error bounds associated with these measurements are not known. However, error bounds of the order of 100 m/s are not uncommon in field experiments.

The lower panel shows the wave speeds vs. brine volume for the summer ice temperature of -5°C. The empirical (solid) curve is computed using Eqs. (5.3), (5.6), and (5.7). Salinity is still varied from 0 to 10 ppt but because of the different equation used in calculating brine volume, brine volume now varies between 0-10 pph (0-10%). The dashed curve is the theoretical prediction of wave speed using effective medium theory. As was the case for the winter, the 0% empirical wave speeds are used as the initial value for the effective medium

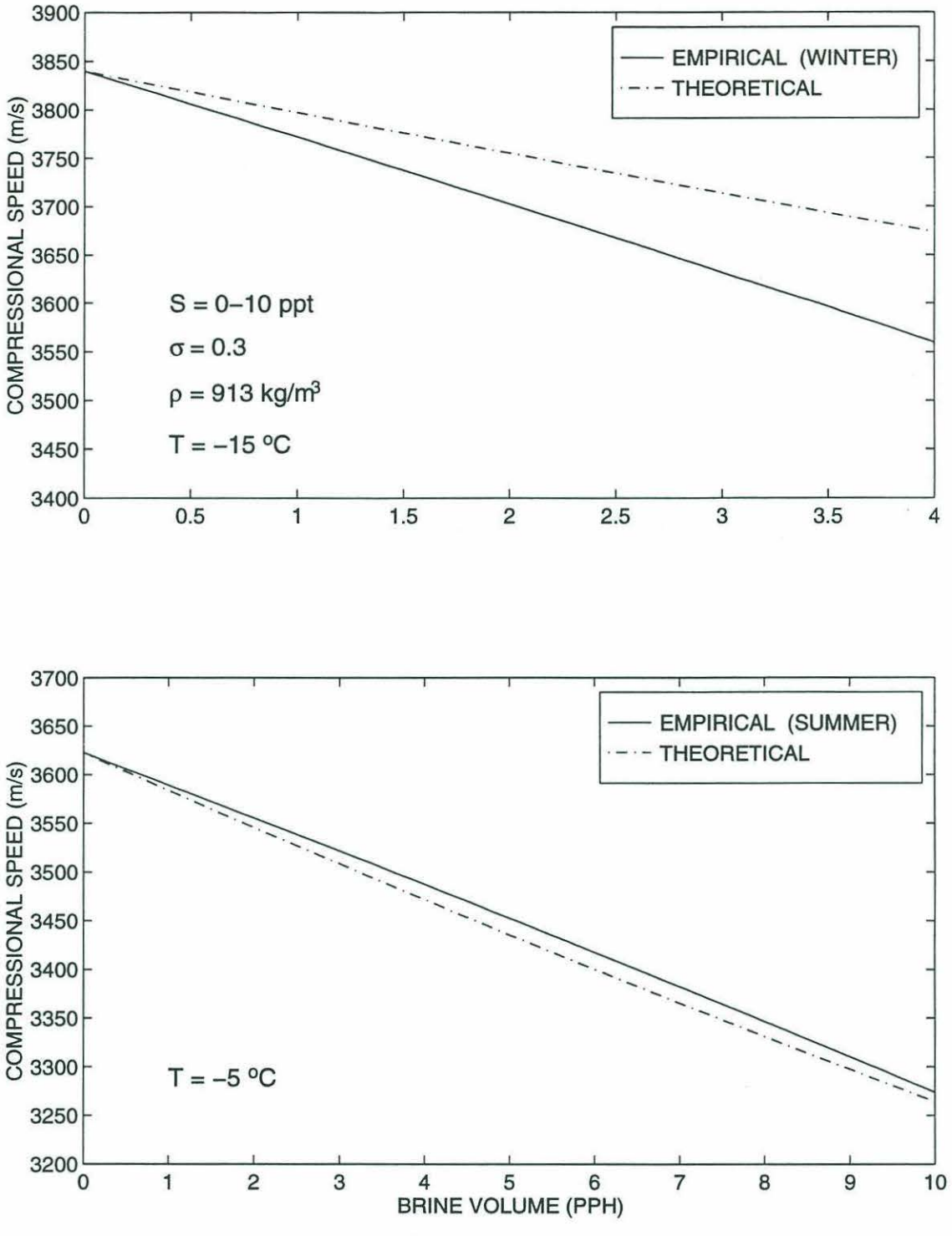

Figure 5-5: Compressional wave speed vs. brine volume for winter and summer values of temperature. Top: winter months with an ice temperature of -15°C Bottom: summer months with an ice temperature of -5°C. Salinity varied from 0-10 ppt, Poisson's ratio (σ) = 0.3, and density (ρ) = 913 kg/m^3.

wave speeds. It is noted that the curves are very close in agreement with less than 0.5% difference at the 10% value of brine volume.

5.5 Effective medium theory vs. tomographic inversion

As a final test of the usefulness of the effective medium theory, wave speeds obtained from tomographic inversion are compared with effective wave speeds from effective medium theory to obtain the percent concentration of inclusions. The theory assumes cylindrical, fluid-filled inclusions.

Rajan *et al.*[25] determined compressional and shear wave speeds in Arctic sea ice by the method of crosshole tomography. Corings were performed at the experimental site and analyzed to determine salinity and temperature as a function of depth. Although the ice was approximately 3 m in depth, a core of 2.2 m was obtained because of difficulty in removing it. Figure 5-6 shows the temperature profile from this core. As a test of the effective medium theory, the temperature data were used to calculate the 0% brine volume content for Young's modulus of elasticity (E). Empirical relations of Young's modulus are given in Eqs. (5.5) and (5.6). Because the definitions of cold and warm sea ice are ambiguous, it was assumed that Young's modulus of elasticity varied linearly between temperatures of $-25°C$ and $-5°C$. This expression is given as:

$$\mathrm{E} = \left(8.9 + \frac{1.1\ (|T| - 0.5)}{24.5}\right) 10^9 \quad (\mathrm{N/m^2}) \tag{5.9}$$

where $\nu = 0$ for 0% brine volume content. The pure ice density ($\mathrm{kg/m^3}$) is calculated using the relation from Pounder [24]

$$\rho_{pure} = 917.0 - 1.403\mathrm{x}10^{-1}T(°C). \tag{5.10}$$

Having calculated the pure ice density and Young's modulus of elasticity, the Lamé parameters λ_{pure} and μ_{pure} can be determined as follows:

$$\mu_{pure} = \frac{\mathrm{E}}{\rho_{pure} 2(1+\sigma)} \tag{5.11}$$

$$\lambda_{pure} = \frac{\mathrm{E}(1-\sigma)}{(1+\sigma)(1-2\sigma)} - 2\mu_{pure}. \tag{5.12}$$

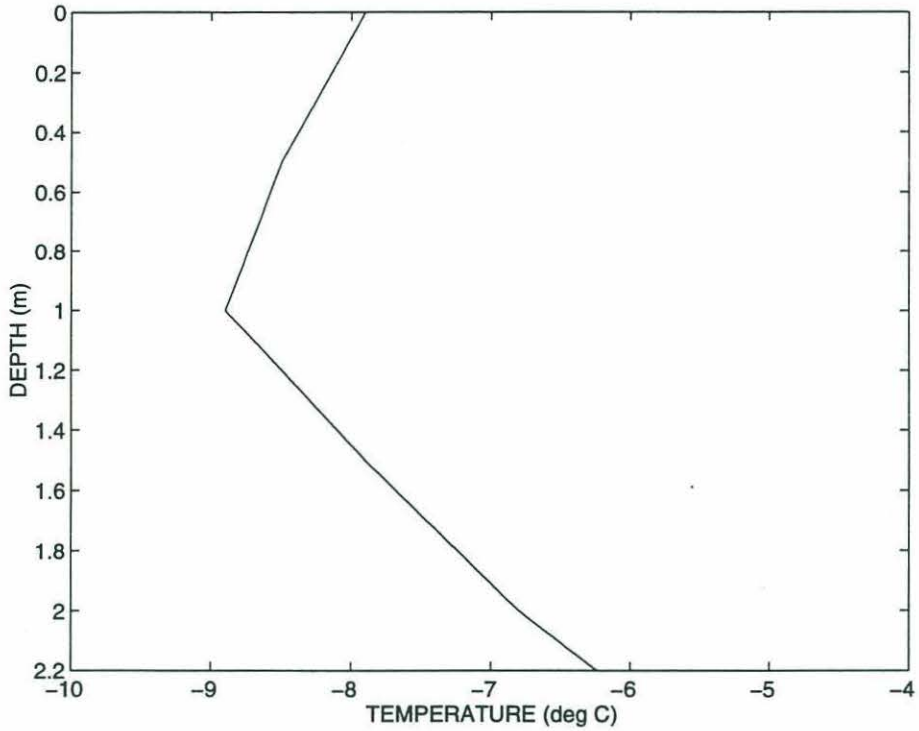

Figure 5-6: Temperature vs. depth profile for sea ice core. (from Rajan *et al.*)

Poisson's ratio (σ) was assumed to be 0.33. Using the temperature profile from Fig. 5-6, the pure ice values from Eqs. (5.11) and (5.12) can be calculated as a function of depth. The effective compressional wave speeds are then calculated as a function of depth for inclusion concentrations varying between 0 and 100%.

The compressional wave speeds in arctic ice obtained from tomographic inversions is shown in the top panel of Fig. 5-7. The compressional wave speed varies from 3100 - 4000 m/s with the depth ranging from 0.6 to 2.2 m. The wave speeds at each depth and range are compared against the effective medium wave speeds to obtain the concentration of inclusions. The concentration values obtained from this comparison are shown in the middle panel of Fig. 5-7. The concentration of inclusions ranges from 0% (high speed region) to 20% (low speed region). The bottom panel of the figure is the brine volume content as a function of depth and range. The brine volume content is determined using Eqs. (5.2) - 5.4 and wave speed (shown in top panel of the figure) and salinity data from Rajan *et al.* [25]. It can be seen by comparing the middle and bottom panels of the figure that effective medium theory can predict regions of high and low porosity using wave speed

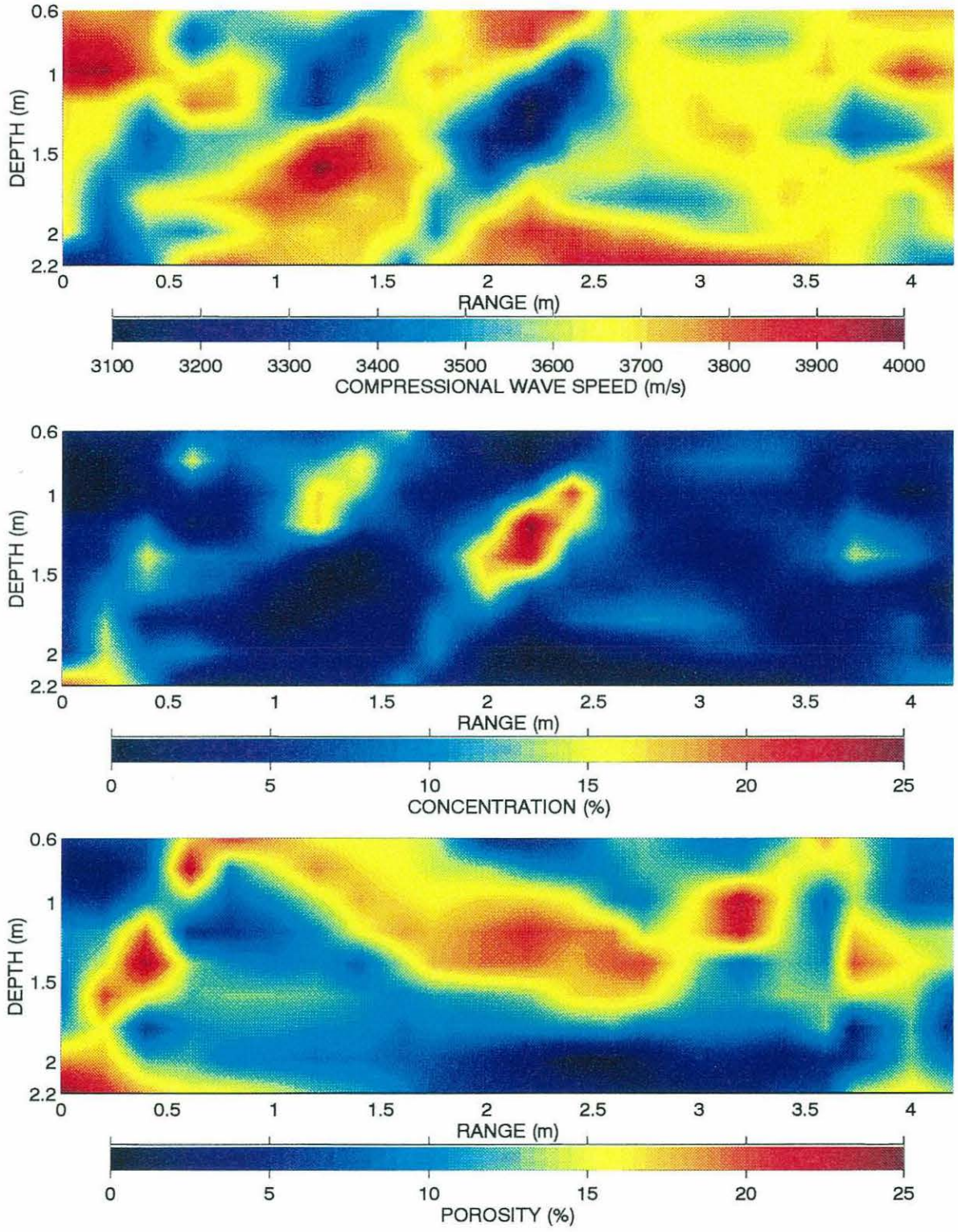

Figure 5-7: Top: compressional wave speeds from tomographic inversion (from Rajan *et al.*). Middle: concentration of inclusions obtained by comparing compressional wave speeds from effective medium theory and those from the panel above. Poisson's ratio = 0.33. Bottom: porosity determined from empirical relationships using temperature, salinity and wave speed data from Rajan *et al.*

data. The region of high porosity at a range of approximately 3.2 m and depth 1.1 m is not found in the middle panel. This is due to using a constant value of Poisson's ratio for determining the pure ice Lamé parameters in the effective medium relations. Although an exact value of porosity cannot be determined, Fig. 5-7 is evidence that an effective medium approach is qualitatively consistent with experimental field data.

Chapter 6

Conclusion

This final chapter summarizes important results from this thesis and provides recommendations on how others can extend the work presented here.

6.1 Scattering from a single cylindrical fluid inclusion

The foundation of this thesis is based on acoustic wave scattering from a fluid inclusion in an attenuating elastic medium. In Chap. 2 scattering theory which is based on an infinite series solution to the wave equation is reviewed. By matching boundary conditions, the unknown modal series coefficients are solved for which are then used to predict the radial displacement field at a point in the far field of the scatterer. The work is unique because it validates the analytic solution by comparison with a laboratory experiment. Polypropylene as a surrogate for ice because it is easier to work with experimentally and has similar acoustic wave speeds as sea ice.

It was found that at low ka values, the scattering vs. angle exhibits a dipole-like structure as shown in Fig. 2-3. As ka increases, the scattered field is essentially concentrated in the forward direction. If one makes a total field measurement (incident + scattered), they would find that there is a shadow zone in the forward direction due to interference between the incident and scattered fields. As one moves toward the backscattered direction ($\theta = \pi$), the field would be primarily due to the incident field. This study also examined the effects of attenuation and found that it made a significant difference in the scattered field.

Results of experimental work validating this theory are presented in Chap. 4. The total displacement field vs. angle was measured for ka values of 1.9, 2.4, 8.8, and 11.0. Excellent

agreement was found qualitatively between the analytic solution and experimental results as can be seen in Figs. 4-3 - 4-6.

6.2 Effective medium theory

Having validated scattering from a single cylindrical fluid-filled inclusion, the development is expanded to include scattering from multiple cylindrical inclusions. The theory is based on work done by Kuster and Toksöz [18] for an aggregate of spheres. The contribution of such a study is unique because an analytical expression for effective moduli for cylindrical inclusions in an elastic medium is developed. Furthermore, the theoretical predictions are validated by experimental work. The following assumptions are made in the theoretical development.

1. Single scattering occurs from each individual cylindrical inclusion. Multiple scattering effects are ignored.
2. The theory is valid at low ka such that the wavelength of the incident acoustic wave is much longer compared to the radius of the cylinder.
3. Measurements are made in the far field.

Once again, polypropylene is used as a surrogate for sea ice in the laboratory experiment. the wave speeds are measured as a function of concentration of cylindrical inclusions. Excellent agreement was found quantitatively at low concentrations. The largest deviation between experimental and theoretical predictions occurred at a concentration of 2.4%. At this concentration the wave speed differed by 0.75% from the predicted. This proves that the effective medium theory is an excellent means of predicting wave speeds given inclusion concentration. The results could be improved further by reducing the frequency of the acoustic source or the size of the inclusions. The laboratory environment and the inability to machine holes small enough limited this study to a ka of 0.35. The theory is valid at $ka \ll 1$ so reducing ka as low as possible will improve the results.

The next and most encouraging results were obtained by comparing effective medium theory compressional wave speeds with predictions using empirical relationships derived from field data. As stated earlier, effective medium theory is applicable for a two phase medium in which the material properties of the individual phases are known. In the experimental work, it was relatively easy to obtain the homogeneous material properties of

polypropylene and water. However, it is virtually impossible to measure the homogeneous material properties of sea ice since it is inhomogeneous by nature. Consequently, to compare effective medium results with sea ice data, one must use the 0% brine inclusion wave speeds to use as initial inputs into the effective medium theory. Empirical relationships are used because they allow one to determine these wave speeds at no brine volume concentrations. These empirical relationships are for Young's modulus elasticity which were measured from four sets of field data by Langleben and Pounder [19]. It is trivial to compute the wave speeds since they are a function of Young's modulus of elasticity, density, and Poisson's ratio.

Excellent agreement between the empirical and effective medium relationships was found. A discrepancy of 4% was found for winter values of Young's modulus and less than 0.5% for summer values.

6.3 Future work

The concept of an effective medium theory is attractive because it provides an easy means of predicting wave speeds in sea ice given the concentration of inhomogeneities such as air pockets or brine channels. The derivation presented here is based on fluid cylinders embedded in an elastic medium such as ice. A more complete theory can be derived in which other inhomogeneities such as cracks or spherical air pockets are accounted for. Kuster and Toköz [18] developed the theory for spherical inclusions and Budiansky and O'Connell [8] developed a theory for cracks. Using a superposition of these theories would allow one to account for varying concentrations of different geometry inhomogeneities. Although an elegant analytic solution would not be possible, the problem could easily be solved numerically.

A second and more exciting possibility of this theory is the study of the effect of anisotropy of a material on wave speed. As a preliminary test, the crosswise compressional wave speed in polypropylene was measured in which 203 holes were drilled (see Chap. 5). The lengthwise compressional wave speed was then measured and found no change from the no-hole wave speed. Experimental work could be performed to determine the change in wave speed as the angle of incidence is changed from broadside to end on. This would be invaluable to acousticians who perform acoustic tomography since sea ice is highly anisotropic.

Lastly, the theory has been validated for predicting compressional wave speeds. The theory is able to predict the change in shear wave speeds as a function of concentration but stills needs to be validated by experimental work.

Appendix A

Solid-Solid Scattering

The solution for scattering from an elastic cylinder embedded in an elastic matrix is required in order to determine the first three scattering coefficients. It is these coefficients which are used in the effective medium derivation as discussed in Chap. 3. Following a similar development for the scattering from a cylindrical fluid-filled inclusion in a solid elastic matrix, a compressional plane wave is incident normal to the axis of the cylinder. At the boundary of the cylinder, there is a scattered compressional and shear wave and a transmitted shear and compressional wave. A shear wave is now transmitted since the elastic cylinder is able to support this type of wave. The potentials which satisfy the Helmholtz equation can be written as follows:

$$\Phi_{inc} = \sum_{n=0}^{\infty} \epsilon_n i^n J_n(k_{p_1} r) \cos(n\theta)$$
$$\Phi_{p_1} = \sum_{n=0}^{\infty} A_n H_n^{(1)}(k_{p_1} r) \cos(n\theta)$$
$$\Psi_{s_1} = \sum_{n=0}^{\infty} B_n H_n^{(1)}(k_{s_1} r) \sin(n\theta)$$
$$\Phi_{p_2} = \sum_{n=0}^{\infty} C_n J_n(k_{p_2} r) \cos(n\theta)$$
$$\Psi_{s_2} = \sum_{n=0}^{\infty} D_n J_n(k_{s_2} r) \sin(n\theta)$$

The subscripts of the potentials $p_{1,2}$, $s_{1,2}$ refer to compressional and shear waves in medium 1 or 2 respectively. The coefficient of the scattered and transmitted potentials are determined from the following boundary conditions

$$u_r^{inc} + u_r^{scatt} = u_r^{trans} \tag{A.1}$$

$$u_\theta^{inc} + u_\theta^{scatt} = u_\theta^{trans} \tag{A.2}$$

$$\tau_{rr}^{inc} + \tau_{rr}^{scatt} = \tau_{rr}^{trans} \tag{A.3}$$

$$\tau_{r\theta}^{inc} + \tau_{r\theta}^{scatt} = \tau_{r\theta}^{trans}. \tag{A.4}$$

These represent continuity of radial displacement, tangential displacement, radial stress, and tangential stress respectively. Note that the elastic-elastic problem can be reduced to the elastic-fluid case by utilizing boundary conditions (A.1), (A.3), and (A.4). Additionally, the D_n coefficients are zero since the fluid is unable to support shear waves.

A.1 Particle Displacement

As before, the particle displacement is defined as:

$$\vec{u} = \nabla\Phi + \nabla \times \mathbf{\Psi}.$$

From the symmetry of the problem, the displacements can be separated into their radial and tangential components.

$$u_r = \frac{\partial\Phi}{\partial r} + \frac{1}{r}\frac{\partial\Psi_z}{\partial\theta} \tag{A.5}$$

$$u_\theta = \frac{1}{r}\frac{\partial\Phi}{\partial\theta} - \frac{\partial\Psi_z}{\partial r}. \tag{A.6}$$

Solving for the radial and tangential displacements for the incident,scattered and transmitted waves yields:

$$u_r^{inc} = \frac{\partial\Phi_{inc}}{\partial r} = \sum_{n=0}^{\infty} \epsilon_n i^n k_{p_1} J_n'(k_{p_1} r)\cos(n\theta)$$

$$u_r^{scatt} = \frac{\partial\Phi_{p_1}}{\partial r} + \frac{1}{r}\frac{\partial\Psi_{s_1}}{\partial\theta} = \sum_{n=0}^{\infty}\left\{A_n k_{p_1} H_n'(k_{p_1} r) + \frac{n}{r}B_n H_n(k_{s_1} r)\right\}\cos(n\theta)$$

$$u_r^{trans} = \frac{\partial\Phi_{p_2}}{\partial r} + \frac{1}{r}\frac{\partial\Psi_{s_2}}{\partial\theta} = \sum_{n=0}^{\infty}\left\{C_n k_{p_2} J_n'(k_{p_2} r) + \frac{n}{r}D_n J_n(k_{s_2} r)\right\}\cos(n\theta)$$

$$u_\theta^{inc} = \frac{1}{r}\frac{\partial \Phi_{inc}}{\partial \theta} = \sum_{n=0}^{\infty} -\frac{n}{r}\epsilon_n i^n J_n(k_{p_1} r)\sin(n\theta)$$

$$u_\theta^{scatt} = \frac{1}{r}\frac{\partial \Phi_{p_1}}{\partial \theta} - \frac{\partial \Psi_{s_1}}{\partial r} = \sum_{n=0}^{\infty}\left\{-A_n\frac{n}{r}H_n(k_{p_1} r) - B_n k_{s_1} H_n'(k_{s_1} r)\right\}\sin(n\theta)$$

$$u_\theta^{trans} = \frac{1}{r}\frac{\partial \Phi_{p_2}}{\partial \theta} - \frac{\partial \Psi_{s_2}}{r} = \sum_{n=0}^{\infty}\left\{-C_n\frac{n}{r}J_n(k_{p_2} r) - D_n k_{s_2} J_n'(k_{s_2} r)\right\}\sin(n\theta)$$

A.2 Normal Stress

The equation for normal stress was given previously in Chap. 2. It is rewritten here for completeness along with the solutions for components of the incident, scattered and transmitted normal stresses.

$$\begin{aligned}\tau_{rr} &= \lambda\nabla\cdot\vec{u} + 2\mu\frac{\partial u_r}{\partial r} \\ &= (\lambda+2\mu)\frac{\partial u_r}{\partial r} + \lambda\left(\frac{u_r}{r} + \frac{1}{r}\frac{\partial u_\theta}{\partial \theta}\right)\end{aligned}$$

$$\frac{\partial u_\theta^{inc}}{\partial \theta} = \sum_{n=0}^{\infty} -\frac{n^2}{r}\epsilon_n i^n J_n(k_{p_1} r)\cos(n\theta)$$

$$\frac{\partial u_\theta^{scatt}}{\partial \theta} = \sum_{n=0}^{\infty}\left\{-A_n\frac{n^2}{r}H_n(k_{p_1} r) - B_n n k_{s_1} H_n'(k_{s_1} r)\right\}\cos(n\theta)$$

$$\frac{\partial u_\theta^{trans}}{\partial \theta} = \sum_{n=0}^{\infty}\left\{-C_n\frac{n^2}{r}J_n(k_{p_2} r) - D_n n k_{s_2} J_n'(k_{s_2} r)\right\}\cos(n\theta)$$

$$\frac{\partial u_r^{inc}}{\partial r} = \sum_{n=0}^{\infty}\epsilon_n i^n k_{p_1}^2 J_n''(k_{p_1} r)\cos(n\theta)$$

$$\frac{\partial u_r^{scatt}}{\partial r} = \sum_{n=0}^{\infty}\left\{A_n k_{p_1}^2 H_n''(k_{p_1} r) + B_n n\left(\frac{k_{s_1}}{r}H_n'(k_{s_1} r) - \frac{H_n(k_{s_1} r)}{r^2}\right)\right\}\cos(n\theta)$$

$$\frac{\partial u_r^{trans}}{\partial r} = \sum_{n=0}^{\infty}\left\{C_n k_{p_2}^2 J_n''(k_{p_2} r) + D_n n\left(\frac{k_{s_2}}{r}J_n'(k_{s_2} r) - \frac{J_n(k_{s_2} r)}{r^2}\right)\right\}\cos(n\theta)$$

A.3 Shear Stress

As was the case for normal stress, the results from Chap. 2 are presented and the components of the incident, scattered and transmitted shear stresses are explicitly solved for.

$$\tau_{r\theta} = \mu \left\{ \frac{\partial u_\theta}{\partial r} - \frac{u_\theta}{r} + \frac{1}{r}\frac{\partial u_r}{\partial \theta} \right\}$$

$$\frac{\partial u_\theta^{inc}}{\partial r} = \sum_{n=0}^{\infty} -n\epsilon_n i^n \left\{ \frac{k_{p_1}}{r} J_n'(k_{p_1} r) - \frac{J_n(k_{p_1} r)}{r^2} \right\} \sin(n\theta)$$

$$\frac{\partial u_\theta^{scatt}}{\partial r} = \sum_{n=0}^{\infty} \left\{ -A_n n \left(\frac{k_{p_1}}{r} H_n'(k_{p_1} r) - \frac{H_n(k_{p_1} r)}{r^2} \right) - B_n k_{s_1}^2 H_n''(k_{s_1} r) \right\} \sin(n\theta)$$

$$\frac{\partial u_\theta^{trans}}{\partial r} = \sum_{n=0}^{\infty} \left\{ -C_n n \left(\frac{k_{p_2}}{r} J_n'(k_{p_2} r) - \frac{J_n(k_{p_2} r)}{r^2} \right) - D_n k_{s_2}^2 J_n''(k_{s_2} r) \right\} \sin(n\theta)$$

$$\frac{\partial u_r^{inc}}{\partial \theta} = \sum_{n=0}^{\infty} -n\epsilon_n i^n k_{p_1} J_n'(k_{p_1} r) \sin(n\theta)$$

$$\frac{\partial u_r^{scatt}}{\partial \theta} = \sum_{n=0}^{\infty} \left\{ -A_n n k_{p_1} H_n'(k_{p_1} r) - B_n \frac{n^2}{r} H_n(k_{s_1} r) \right\} \sin(n\theta)$$

$$\frac{\partial u_r^{trans}}{\partial \theta} = \sum_{n=0}^{\infty} \left\{ -C_n n k_{p_2} J_n'(k_{p_2} r) - D_n \frac{n^2}{r} J_n(k_{s_2} r) \right\} \sin(n\theta)$$

A.4 Modal series coefficients

Boundary conditions defined in Eqs. (A.1) - (A.4) are evaluated at the surface of the cylinder, $r = a$. The resulting equations can be written in matrix form XY = E to solve for the unknown coefficients $A_n, B_n, C_n,$ andD_n. Specifically, they can be written as:

$$\begin{bmatrix} x_{11} & x_{12} & x_{13} & x_{14} \\ x_{21} & x_{22} & x_{23} & x_{24} \\ x_{31} & x_{32} & x_{33} & x_{34} \\ x_{41} & x_{42} & x_{43} & x_{44} \end{bmatrix} \begin{bmatrix} A_n \\ B_n \\ C_n \\ D_n \end{bmatrix} = \begin{bmatrix} E_1 \\ E_2 \\ E_3 \\ E_4 \end{bmatrix} \tag{A.7}$$

where the elements of the X matrix and D vector are given by:

$$
\begin{aligned}
x_{11} &= k_{p_1} a H_n'(k_{p_1} a) \\
x_{12} &= n H_n(k_{s1} a) \\
x_{13} &= -k_{p_2} a J_n'(k_{p_2} a) \\
x_{14} &= -n J_n(k_{s_2} a)
\end{aligned}
$$

$$
\begin{aligned}
x_{21} &= n H_n(k_{p_1} a) \\
x_{22} &= k_{s_1} a H_n'(k_{s_1} a) \\
x_{23} &= -n J_n(k_{p_2} a) \\
x_{24} &= -k_{s_2} a J_n'(k_{s_2} a)
\end{aligned}
$$

$$
\begin{aligned}
x_{31} &= H_n(k_{p_1} a)(2n^2 - k_{s1}^2 a^2) - 2k_{p_1} a H_n'(k_{p_1} a) \\
x_{32} &= 2n(k_{s1} a H_n'(k_{s1} a) - H_n(k_{s1} a)) \\
x_{33} &= \left(\frac{\rho_2}{\rho_1} k_{s_1}^2 a^2 - 2n^2 \frac{\rho_2}{\rho_1} \frac{k_{s_1}^2}{k_{s_2}^2} \right) J_n(k_{p_2} a) + 2 \frac{\rho_2}{\rho_1} \frac{c_{s_2}^2}{c_{s_1}^2} k_{p_2} a J_n'(k_{p_2} a) \\
x_{34} &= 2n \frac{\rho_2}{\rho_1} \frac{k_{s_1}^2}{k_{s_2}^2} \left(J_n(k_{s_2} a) - k_{s_2} a J_n'(k_{s_2} a) \right)
\end{aligned}
$$

$$
\begin{aligned}
x_{41} &= 2n(H_n(k_{p_1} a) - k_{p_1} a H_n'(k_{p_1} a)) \\
x_{42} &= 2k_{s1} a H_n'(k_{s1} a) + (k_{s1}^2 a^2 - 2n^2) H_n(k_{s1} a) \\
x_{43} &= \frac{\rho_2}{\rho_1} \frac{k_{s_1}^2}{k_{s_2}^2} 2n \left(k_{p_2} a J_n'(k_{p_2} a) - J_n(k_{p_2} a) \right) \\
x_{44} &= \frac{\rho_2}{\rho_1} \frac{k_{s_1}^2}{k_{s_2}^2} \left(J_n(k_{s_2} a)(2n^2 - k_{s_2}^2 a^2) - 2k_{s_2} a J_n'(k_{s_2} a) \right)
\end{aligned}
$$

$$
\begin{aligned}
E_1 &= -\epsilon_n i^n k_{p_1} a J_n'(k_{p_1} a) \\
E_2 &= -n \epsilon_n i^n J_n(k_{p_1} a) \\
E_3 &= -\epsilon_n i^n \left((2n^2 - k_{s1}^2 a^2) J_n(k_{p_1} a) - 2k_{p_1} a J_n'(k_{p_1} a) \right) \\
E_4 &= \epsilon_n i^n 2n(k_{p_1} a J_n'(k_{p_1} a) - J_n(k_{p_1} a))
\end{aligned}
$$

The following relations from Abramowitz and Stegun [1] have been used:

$$z^2 H_n'' = (n^2 - z^2) H_n(z) - z H_n'(z)$$

$$z^2 J_n'' = (n^2 - z^2) J_n(z) - z J_n'(z)$$

Appendix B

Derivation of Effective Medium Scattering Coefficients

The compressional wave scattering coefficients A_n are derived by matching boundary conditions at the cylindrical surface $r = a$. For low ka values, it has been shown [28] that the first three terms ($A_o, A_1,$ andA_2) are the significant contributors to the total field. A_n is computed since radial contributions to the scattered field for the compressional waves are of interest. This is justified because the experimental work of this study utilized compressional wave transducers.

B.1 A_o

Cramer's Rule is used to solve for A_o to arrive at the following equation:

$$A_o^{num} = \left(\frac{\rho_2}{\rho_1} k_{s_1}^2 a^2 J_o(k_{p_2} a) + 2\frac{\rho_2}{\rho_1}\frac{c_{s_2}^2}{c_{s_1}^2} k_{p_2} a J_o'(k_{p_2} a)\right)(-k_{p_1} a J_o'(k_{p_1} a)) - (k_{p_2} a J_o'(k_{p_2} a))(-k_{s_1}^2 a^2 J_o(k_{p_1} a) - 2k_{p_1} a J_o'(k_{p_1} a)) \quad \text{(B.1)}$$

$$A_o^{den} = k_{p_1} a H_o'(k_{p_1} a)\left(\frac{rho_2}{\rho_1} k_{s_1}^2 a^2 J_o(k_{p_2} a) + 2\frac{\rho_2}{\rho_1}\frac{c_{s_2}^2}{c_{s_1}^2} k_{p_2} a J_o'(k_{p_2} a)\right) - k_{p_2} a J_o'(k_{p_2} a)(k_{s_1}^2 a^2 H_o(k_{p_1} a) + 2k_{p_1} a H_o'(k_{p_1} a)). \quad \text{(B.2)}$$

A_o^{num} and A_o^{den} are the numerator and denominator of A_o. The small argument formulas for the Hankel and Bessel functions [1]

$$J_o(z) \sim 1 \quad H_o(z) \sim 1 + \frac{2i}{\pi} ln(z)$$
$$J_1(z) \sim \frac{z}{2} \quad zH_1(z) \sim \frac{z^2}{2} - \frac{2i}{\pi}$$

are utilized to arrive at:

$$A_o = \frac{k_{p_1}^2 a^2 (\frac{\rho_2}{\rho_1}(k_{s_1}^2 a^2 - \frac{c_{s_2}^2}{c_{s_1}^2} k_{p_2}^2 a^2) - \frac{k_{p_2}^2 a^2 k_{s_1}^2 a^2}{k_{p_1}^2 a^2} + k_{p_2}^2 a^2)}{\frac{4i}{\pi}(\frac{\rho_2}{\rho_1}(k_{s_1}^2 a^2 - \frac{c_{s_2}^2}{c_{s_1}^2} k_{p_2}^2 a^2) + k_{p_2}^2 a^2)}. \tag{B.3}$$

Equation (B.3) was arrived at by neglecting higher order terms $(ka)^4$ since $ka \ll 1$ for $k_{p_1}a$, $k_{s_1}a$, $k_{p_2}a$, and $k_{s_2}a$. The following substitutions are made:

$$k_p^2 a^2 = \frac{w^2 a^2}{c_p^2} = \frac{\rho w^2 a^2}{\lambda + 2\mu} \tag{B.4}$$

$$k_s^2 a^2 = \frac{w^2 a^2}{c_s^2} = \frac{\rho w^2 a^2}{\mu} \tag{B.5}$$

to yield the final result:

$$A_o \sim -k_{p_1}^2 a^2 \frac{\pi}{4} i \left\{ \frac{\lambda_2 + \mu_2 - \lambda_1 - \mu_1}{\lambda_2 + \mu_2 + \mu_1} \right\}. \tag{B.6}$$

λ and μ are Lamé parameters, w is the radial frequency, a is the radius of the cylindrical inclusion and the subscripts 1,2 apply to the surrounding matrix and inclusion respectively.

B.2 A_1

The solution to A_1 is arrived at by using Cramer's rule as before. The numerator of A_1 resulted from neglecting terms $O((ka)^8)$ whereas the denominator resulted from neglecting terms $O((ka)^6)$. The solution is listed below:

$$A_1^{num} = -\frac{1}{\pi} \frac{\rho_2^2}{\rho_1^2} \left(1 - \frac{\rho_1}{\rho_2}\right) k_{s_1}^3 a^3 k_{p_2} a k_{s_2} a k_{p_1} a \tag{B.7}$$

$$A_1^{den} = \frac{4}{\pi^2} \frac{\rho_2}{\rho_1} k_{s_1}^3 a^3 \frac{k_{p_2} a}{k_{p_1} a} k_{s_2} a. \tag{B.8}$$

Making the substitution

$$A_1 = \frac{A_1^{num}}{A_1^{den}}$$

yields the final approximate solution to A_1

$$A_1 \sim \frac{\pi}{4} k_{p_1}^2 a^2 \left(\frac{\rho_1 - \rho_2}{\rho_1} \right). \tag{B.9}$$

B.3 A_2

The solution to A_2 is similar to the derivations in the preceding sections by letting $n = 2$. The intermediate result for A_2 is presented below:

$$A_2 = \frac{k_{p_1}^2 a^2 k_{p_2}^2 a^2 \frac{i}{\pi} \frac{\rho_2}{\rho_1} \left(\frac{\rho_2}{\rho_1} k_{s_1}^2 a^2 - k_{s_2}^2 a^2 \right)}{\frac{2}{\pi^2} \frac{\rho_2}{\rho_1} k_{p_2}^2 a^2 \left(\frac{\rho_2}{\rho_1} \frac{k_{s_1}^4 a^4}{k_{p_1}^2 a^2} + \frac{\rho_2}{\rho_1} k_{s_1}^2 a^2 + \frac{k_{s_1}^2 a^2 k_{s_2}^2 a^2}{k_{p_1}^2 a^2} - k_{s_2}^2 a^2 \right)} \tag{B.10}$$

In this derivation, higher order terms $O((ka)^8)$ were neglected in the numerator and $O((ka)^6)$ terms were neglected for the denominator. After substituting the relations (B.4) and (B.5) into (B.10) and simplifying, the final approximate solution to A_2 is:

$$A_2 \sim \frac{k_{p_1}^2 a^2 \frac{\pi}{4} i(\mu_2 - \mu_1) 2\mu_1}{(\lambda_1 + 2\mu_1)(\mu_2 + \mu_1) + \mu_1 \mu_2 - \mu_1^2}. \tag{B.11}$$

Bibliography

[1] M. Abramowitz and I. A. Stegun, ed., *Handbook of Mathematical Functions with Formulas, Graphs, and Mathematical Tables*, National Bureau of Standards: Applied Mathematics Series, issued June 1964; tenth printing, Dec. 1972.

[2] J. D. Achenbach, *Wave Propagation in Elastic Solids*, North-Holland Pub. Co., Amsterdam, 1973.

[3] R. C. Addison, Jr. and A. N. Sinclair, "Calculated and measured ultrasonic response of an elastic cylinder embedded in an elastic medium," *Rev. Prog. Non-Destruct. Eval.*, **11a**, 105–111, 1991.

[4] D. E. Amos, "Algorithm 644: a portable package for bessel functions of a complex argument and non-negative order," *ACM Trans. Math. Soft.*, **12**, 265–273, 1986.

[5] P. Beattie, R. C. Chivers, and L. W. Anson, "Ultrasonic backscattering from solid cylindrical inclusions in solid elastic matrices: A comparison of theory and experiment," *J. Acoust. Soc. Am.*, **94**, 3421–3427, 1993.

[6] J. G. Berryman, "Long-wavelength propagation in composite elastic media 1. Spherical inclusions," *J. Acoust. Soc. Am.*, **68**, 1809–1819, 1980.

[7] B. Budiansky, "On the elastic moduli of some heterogeneous materials," *J. Mech. Phys. Solids*, **13**, 223–227, 1965.

[8] B. Budiansky and R. J. O'Connell, "Elastic moduli of a cracked solid," *Int. J. Solids Struct.*, **12**, 81–97, 1976.

[9] C. F. DuToit, "The numerical computation of bessel functions of the first and second kind for integer orders and complex arguments," *IEEE Trans. Anten. Prop.*, **38**, 1341–1349, 1990.

[10] J. J. Faran, Jr., "Sound scattering by solid cylinders and spheres," *J. Acoust. Soc. Am.*, **23**, 405–418, 1951.

[11] G. Frankenstein and R. Garner, "Equations for determining the brine volume of sea ice from $-.5°$ to $-22.9°$ C.," *J. Glaciol.*, **48**, 943–944, 1967.

[12] J. R. Fricke and G. L. Unger, "Acoustic scattering from elemental Arctic ice features: experimental results," *J. Acoust. Soc. Am.*, **97**, 192–198, 1995.

[13] B. Hartmann and J. Jarzynski, "Immersion apparatus for ultrasonic measurements in polymers," *J. Acoust. Soc. Am.*, **56**, 1469–1477, 1974.

[14] Z. Hashin and S. Shtrikman, "Note on a variational approach to the theory of composite elastic materials," *J. Franklin Inst.*, **271**, 336–341, 1961.

[15] F. B. Hildebrand, *Advanced Calculus for Applications, 2nd ed.*, Prentice-Hall Inc., New Jersey, 1976.

[16] R. Hill, " A self-consistent mechanics of composite materials," *J. Mech. Phys. Solids*, **13**, 213–222, 1965.

[17] Y. Kim, B. Lee, and J. Ih, "Scattering of longitudinal waves by a cylindrical cavity in an attenuating solid," *J. Acoust. Soc. Am.*, **93**, 93–101, 1993.

[18] G. T. Kuster and M. N. Toksöz, "Velocity and attenuation of seismic waves in two-phase media: part 1. Theoretical formulations," *Geophys.*, **39**, 587-606, 1974.

[19] M. P. Langleben and E. R. Pounder, "Elastic parameters of sea ice," in *Ice and Snow; Properties, Processes and Applications*, Proceedings of a conference held 12-16 February 1963, at MIT Cambridge, MA (MIT, Cambridge, MA, 1963), pp. 69–78.

[20] W. H. Lin and A.C. Raptis, "Acoustic scattering by elastic solid cylinders and spheres in viscous fluids," *J. Acoust. Soc. Am.*, **73**, 736–748, 1983.

[21] A. E. H. Love, *The mathematical theory of elasticity*, Dover Publications, New York, fourth edition, 1944.

[22] D. F. McCammon and S. T. McDaniel, "The influence of the physical properties of ice on reflectivity," *J. Acoust. Soc. Am.*, **77**, 499–507, 1985.

[23] P. M. Morse and K. U. Ingard, *Theoretical Acoustics*, McGraw-Hill, New York, 1968.

[24] E. R. Pounder, *The Physics of Ice*, Pergamon Press Inc., New York, 1965.

[25] S. D. Rajan, G. V. Frisk, J. A. Doutt, and C. J. Sellers, "Determination of compressional wave and shear wave speed profiles in sea ice by crosshole tomography – theory and experiment," *J. Acoust. Soc. Am.*, **93**, 721–738, 1993.

[26] Lord Rayleigh, *The theory of sound*, Dover Publications, New York, 1945.

[27] D. C. Ricks, *Elastodynamic modeling of fluid-loaded cylindrical shells with multiple layers and internal attachments*, Ph.D. thesis, Massachusetts Institute of Technology, 1994.

[28] T. K. Stanton, "Sound scattering by cylinders of finite length. I. Fluid cylinders," *J. Acoust. Soc. Am.*, **83**, 55–63, 1988.

[29] R. J. Urick, *Principles of underwater sound for engineers*, McGraw-Hill, New York, 1975.

[30] L. J. Walpole, "On the overall elastic moduli of composite materials," *J. Mech. Phys. Solids*, **17**, 235–251, 1969.

[31] J. P. Watt, G. F. Davies, and R. J. O'connell, "The elastic properties of composite materials," *Rev. Geophys. Space Phys.*, **14**, 541-563, 1976.

[32] W. F. Weeks and S. F. Ackley, "The growth, structure and properties of sea ice," *CRREL Monograph*, **82-1**, 1982.

[33] R. M. White, "Elastic wave scattering at a cylindrical discontinuity in a solid," *J. Acoust. Soc. Am.*, **30**, 771–785, 1958.